Università Politecnica delle Marche
Dottorato di Ricerca in Ingegneria dell'Informazione
Curriculum "Ingegneria Informatica, Gestionale e dell' Automazione"

Embedded Strategies for Electromechanical Systems

Ph.D. Dissertation of:
Luigi Colombo

Advisor:
Prof. Giuseppe Orlando

Coadvisor:
Prof. Gianluca Ippoliti

Prof. Andrea Serrani

Curriculum Supervisor:
Prof. Francesco Piazza

XXXI edition

Università Politecnica delle Marche
Dottorato di Ricerca in Ingegneria dell'Informazione
Curriculum "Ingegneria Informatica, Gestionale e dell' Automazione"

Embedded Strategies for Electromechanical Systems

Ph.D. Dissertation of:
Luigi Colombo

Advisor:
Prof. Giuseppe Orlando

Coadvisor:
Prof. Gianluca Ippoliti

Prof. Andrea Serrani

Curriculum Supervisor:
Prof. Francesco Piazza

XXXI edition

Università Politecnica delle Marche
Dottorato di Ricerca in Ingegneria dell'Informazione
Facoltà di Ingegneria
Via Brecce Bianche 12 – 60131 Ancona (AN), Italy

To my nephew Antonio.

A mio nipote Antonio.

Abstract

The research activity presented in this thesis concerns the design and development of embedded solutions for electromechanical processes in order to obtain optimised control performances. In detail, *the rotary* permanent magnets synchronous motor and *the linear* piezoelectric motor are the processes that have been studied and deepened in this thesis. For the first process, a “sensorless” technique has been developed, without the aid of mechanical transducers. A sliding mode control, model base technique, has been designed combining a new approach which determines the parameter uncertainty of the model, *i.e.* the stator resistance, and the initial condition of an unmeasured state, *i.e.* the angular position of the rotor.

Then an optimal control technique has been employed to optimise the behaviour of the piezoelectric motor. To this purpose, the Linear Quadratic Gaussian (LQG) control based on a numerically identified model has been used with a view to increasing the performances of the overall system. Following the idea of Reference Governor, the LQG controller regulates a pre-compensated Piezoelectric Actuator (PA) system manipulating the reference signals.

In recent years, considerable progress have been made in robust nonlinear control techniques, such as non-linear adaptive control, control based on the geometric approach, the backstepping and sliding mode control for instance, which take into account the uncertainties in the synthesis phase, ensuring the achievement of the objective control in the face of modelling errors. The sliding control technique is generally recognised as very robust, but the so-called “chattering phenomenon” has given rise to a certain scepticism on this approach. Nowadays, the control strategies are implementable with the availability of powerful low-cost microprocessors.

Sommario

L'attività di ricerca presentata in questa tesi riguarda la progettazione e lo sviluppo di soluzioni embedded per processi elettromeccanici al fine di ottenere prestazioni di controllo ottimizzate. In dettaglio, il motore *rotante* sincrono a magneti permanenti e il motore *lineare* piezoelettrico sono i processi che sono stati studiati e approfonditi in questa tesi. Per il primo processo è stata sviluppata una tecnica "sensorless" senza l'ausilio di trasduttori meccanici. Un controllo di tipo Sliding Mode, tecnica basata su modello, è stato progettato combinando un nuovo approccio che determina l'incertezza dei parametri del modello, *i.e.* la resistenza statorica e la condizione iniziale di uno stato non misurato, *i.e.* la posizione angolare del rotore.

Quindi è stata impiegata una tecnica di controllo ottimale per ottimizzare il comportamento del motore piezoelettrico. A tale scopo è stato utilizzato il controllo LQG basato su un modello numerico identificato, al fine di aumentare le prestazioni dell'intero sistema. Seguendo l'idea del Reference Governor, il controller LQG regola un sistema PA pre-compensato che manipola i segnali di riferimento.

Negli ultimi anni sono stati compiuti notevoli progressi in riguardo alle tecniche di controllo non lineare robuste, come il controllo adattivo, il controllo basato sull'approccio geometrico, il controllo di tipo backstepping e sliding, ad esempio, che tengono conto delle incertezze nella fase di sintesi, e che garantiscono il raggiungimento dell'obbiettivo di controllo dinanzi a errori di modellazione. La tecnica di controllo Sliding è generalmente conosciuta per la sua robustezza, ma il cosiddetto "fenomeno del chattering" ha dato origine a un certo scetticismo su tale approccio. Al giorno d'oggi, queste strategie di controllo sono implementabili con la disponibilità di potenti microprocessori a basso costo.

Acronyms

bEMF back-Electro-Motive Force

DC Direct Current

DOF Degree Of Freedom

DSP Digital Signal Processor

FOC Field Oriented Control

FT Fault-Tolerant

HF high-frequency

ISE Integral Square Error

KCL Kirchhoff Current Law

KF Kalman Filter

KVL Kirchhoff Voltage Law

LMI Linear Matrix Inequalities

LQR Linear Quadratic Regulator

LQG Linear Quadratic Gaussian

LTI Linear Time-Invariant

MIMO Multi-Input Multi-Output

MPC Model Predictive Control

MRC Maxwell Resistive Capacitor

NRMSE Normalised Root Mean Square Error

PAs Piezoelectric Actuators

PID Proportional-Integral-Derivative

PMSMs Permanent Magnet Synchronous Motors

QP Quadratic Programming

RG Reference Governor

RP Rapid Prototyping

SISO Single-Input Single-Output

Contents

1. Summary of PhD Research Activities **1**
1.1. Publications 3
1.2. Structure of the Thesis 4

2. Preliminaries **5**
2.1. Notation 5
2.2. Definitions 5
2.3. Remarks 8
2.4. Theorems 9

I. White-Box Approach **11**

3. Introduction **13**
3.1. Problem statement 15

4. Permanent Magnet Synchronous Motor **17**
4.1. Electrical subsystem 19
4.1.1. The three-phase model, “abc” reference frame 19
4.1.2. Reduced model, “$\alpha\beta$” reference frame 20
4.1.3. Reduced model, “dq” reference frame 21
4.2. Mechanical subsystem 21
4.3. Assumptions 22

5. On-line Determination of (θ_0, ΔR) and Control Design **25**
5.1. The unknowns (θ_0, ΔR) 25
5.1.1. Multiple solutions: a decision algorithm 28
5.1.2. Numerical solution algorithm for DSP implementation . 30
5.2. Sliding Mode Control design 34
5.2.1. Derivation of rotor angular position from currents . . . 34
5.2.2. The sensorless speed-tracking controller 35

6. Setup and Results **39**
6.1. Experimental setup 39
6.2. Results 41
6.2.1. Flops overview 45

II. Black-Box Approach **47**

7. Introduction **49**
7.1. Problem statement 50

8. The Mathematical Model and Control Design **51**
8.1. The hysteresis 51
8.2. Identification of the pre-compensated system 52
8.3. LQG design 55

9. Setup and Results **57**
9.1. Experimental setup 57
9.2. Results 58

10. Conclusions **63**

A. Tips on PMSM Model Parameters **65**
A.1. The winding inductance “L” and the resistance “R” 65
A.2. bEMF constant 65

List of Figures

2.1. a)Balanced three-phase system; b)Transformation of three-phase system into two-phase orthogonal one. 7

4.1. PMSM cross section. 17
4.2. The interconnection between the mechanic and electric dynamics. 18
4.3. The equivalent circuit of the stator. 19

5.1. Flow chart for numerical solution. 31
5.2. Graphical representation of the system (5.16), case ($\theta_e = 0$, $\Delta R = 0$) 32
5.3. The true intersection point of the Fig. 5.2 32
5.4. Graphical representation of the system (5.16), case ($\theta_e = 0$, $\Delta R = +10\%$ of $\bar{R}$) 33
5.5. The true intersection point of the Fig. 5.4 33

6.1. Hardware setup. 39
6.2. Block scheme of the sensorless control. 41
6.3. Signals used to drive open loop the motor, u_α (continuous blue-line) and u_β (dashed red-line). 42
6.4. (a): speed tracking with a trapezoidal reference, ω^* (continuous black-line) and $D_\delta^- \theta_e$ (dashed blue-line); (b) and (c): zoom of the behaviours of the sensorless control under torque disturbances. 43
6.5. (a): control inputs u_α (continuous blue-line) and u_β (dashed red-line) for the trapezoidal reference; (b) and (c): control inputs due to the torque disturbances; (d): control inputs due to the resistance variation. 43
6.6. (a): speed tracking with a sinusoidal reference, ω^* (continuous black-line) and $D_\delta^- \theta_e$ (dashed blue-line); (b) and (c): zoom of the behaviours of the sensorless control under torque disturbances. 44
6.7. (a) control inputs u_α (continuous blue-line) and u_β (dashed red-line) for the sinusoidal reference; (b) and (c): control inputs due to the torque disturbances; (d): control inputs due to the resistance variation. 44

8.1. Identification test results, with step input signals. 54

8.2. Identification test results, with step input signals. 54
8.3. LQG+PI control scheme of the pre-compensated PAs system. . 56

9.1. Experimental setup. 57
9.2. Simulation comparison between PI and LQG+PI outputs. . . . 59
9.3. Simulation comparison between PI and LQG+PI control efforts. 59
9.4. Experimental comparison between PI and LQG+PI outputs. . 60
9.5. Experimental comparison between PI and LQG+PI control efforts. 60

List of Tables

6.1. Technosoft$^{©}$ MBE.300.E500 PMSM parameters. 40
6.2. Numerical solutions. 42

9.1. Controller specifications for simulation and experimental tests. 58
9.2. Simulation results: comparison of PI and LQG+PI under step variations. 61
9.3. Experimental results: comparison of PI and LQG+PI under step variation. 61

A.1. Converter. 66

Chapter 1.

Summary of PhD Research Activities

This thesis resumes the activities performed by the author during his PhD in the triennium 2015-2018, at the Department of Information Engineering of the "Università Politecnica Delle Marche" (UNIVPM). The thesis is focused on the development of embedded strategies for electromechanical systems. Theoretical analysis and experimental results are reported, presenting developed controllers. Two real-world case studies have been considered for testing the proposed strategies: *a rotary motor* and *a linear piezoelectric actuator*. The control systems have been designed according to the model-based paradigm, considering both black-box and white-box approaches [1]. This classification splits the thesis into two parts, where case-studies are considered separately.

A brushless motor has been considered to test an innovative sensorless developed control algorithm. The algorithm allows to estimate non-measured physical variables, *i.e.* angular position and speed of the rotor [2], by studying the dynamic model of the motor. In particular, the sensorless approach has been tested considering the uncertainty reconstruction of the electric parameter of the real model as well as the initial condition of the unmeasured state, *i.e.* the winding resistance and the rotor angular position. As already, the full knowledge of the structure of the mathematical model and of its parameters plays a fundamental role in the model-based nonlinear control theory. Unfortunately, it only works in the ideal world made of simulations and calculus on papers. To get around these inconveniences, a sliding mode control has been designed, by definition, this type of nonlinear control is robust to uncertain on the model and or its parameters [3].

The second part of the thesis considers a black-box modelling approach to design a control system. A piezo system has been considered for developing a non-invasive strategy that allows the improving of the commercial PI pre-compensated system performances through an external control loop. The plant has been identified in the form of a Multi-Input Multi-Output (MIMO) Linear Time-Invariant (LTI) model, exploiting the linear behaviour of the actuated axes. In such systems like the PAs commercial applications, it is preferred to maintain provided PI controllers, avoiding to replace it with advanced alternative regulators, because of: *i*) usually PAs systems' stakeholders do not consider positioning accuracy improvable, *ii*) theoretically PI could be tuned to provide an arbitrary small response time, but finally the controller implementation results impossible for high gains [4]. The proposed solution has been selected to become an advertise to rapid prototyping [5] through the open software Scilab/xCos [6].

This thesis proposes a novel approach to reconstruct an uncertain parameter and the initial condition of an unmeasured state applied to the brushless motor. In addition, the aim is to increase performances of the piezo system without invasive changes to the device.

1.1. Publications

From the above research activities, the following publications have been obtained:

- Journal
  - Colombo, L., Corradini, M. L., Cristofaro, A., Ippoliti, G., and Orlando, G. *"An embedded strategy for online identification of PMSM parameters and sensorless control."*
    IEEE Transactions on Control Systems Technology.
    Full Paper (20 August 2018).
    DOI: 10.1109/TCST.2018.2862415
  - Colombo, L., Corradini, M. L., Ippoliti, G., and Orlando, G. *"Pitch angle control of a wind turbine operating above the rated wind speed: a sliding mode control approach."*
    ISA Transactions
    (UNDER REVIEW)
  - Colombo, L., Corradini, M. L., Ippoliti, G., Orlando, G, and Serrani, A. *"An optimal field-weakening control strategy."*
    IEEE Transactions on Industrial Electronics
    (ON GOING)
- Conference Proceeding
  - Colombo L., Corradini M. L., Cristofaro A., Ippoliti G., and Orlando G. *"A robust sensorless control for PMSM with online parameter identification."*
    In IEEE 15th International Workshop on Variable Structure Systems (VSS), 2018 (pp. 450-454).
    DOI: 10.1109/VSS.2018.8460467
  - Cavanini L., Colombo L., Ippoliti G. and Orlando G. *âĂIJDevelopment and experimental validation of a LQG control for a pre-compensated multi-axis piezo system.âĂİ*
    In IEEE 26th International Symposium on Industrial Electronics (ISIE), 2017 (pp. 460-465).
    DOI: 10.1109/ISIE.2017.8001290
  - Colombo L., Corradini M. L., Cristofaro A., Ippoliti G., and Orlando G. *"A DSP-based robust sensorless speed control for PMSMs."*
    The 42nd Annual Conference of the IEEE Industrial Electronics Society (IECON), 2016 (pp. 6663-6668).
    DOI: 10.1109/IECON.2016.7793048

1.2. Structure of the Thesis

This thesis is divided into two fundamental parts, namely: **Part I White Box approach**, in which the focus is on permanent magnet synchronous motor. In this case study, the knowledge of its mathematical model has been exploited. **Part II Black Box approach**, also a model-based technique has been developed, but contrary to the Part I, through input/output acquired data a numerical model has been identified. Both pieces are self-contained, but for fluency in reading and understanding, it is recommended to read **Chapter 2** because it deals with the notation used throughout the thesis and some mathematical preliminaries.

More specifically, as for the Part I, **Chapter 3** reviewers the state of the art and recent developments about of speed-sensorless of the brushless AC motor. **Chapter 4** addresses the mathematical modelling in three-phase representation, and its two reduced models are derived and explained. **Chapter 5** presents the innovative and tailored algorithm to reconstruct information about a parameter of the mathematical model and its initial condition of an unmeasured state and also the control design. In **Chapter 6**, the experimental results performed in the laboratory are reported.

Part II is organised as follows, **Chapters 7** gives an overview of piezoelectric actuators. **Chapter 8** describes the mathematical model and explains how the numerical model has been obtained. In addition, the control design is also explained. **Chapter 9** shows the simulation and experimental results. Finally, conclusions and future work are summarised in **Chapter 10**.

Chapter 2.

Preliminaries

For the ease of the reader, this chapter goes over some basic mathematical preliminaries that will be used in the rest of the thesis. For a detailed discussion on them, please refer to textbooks [7–10].

2.1. Notation

Let $\mathbb{R}^n$ denote the set of real vectors of dimension n and $\mathbb{N}$ the set of natural integers, respectively. Let $\mathcal{I} \subset \mathbb{N}$ be a finite set of integers. For a vector $\boldsymbol{v} \in \mathbb{R}^n$, v_i denotes the i-th entry of $\boldsymbol{v}$. For a matrix $\boldsymbol{A} \in \mathbb{R}^{n\times m}$, $\boldsymbol{A}^T$ denotes its transpose. The $n \times n$ identity matrix, denoted $\boldsymbol{I}(n)$. For a square matrix $\boldsymbol{A} \in \mathbb{R}^{n\times n}$, $\boldsymbol{A}^{-1}$ denotes its inverse, if it exists. Given a function $f(x) : \mathbb{R}^n \to \mathbb{R}$, $\textbf{dom}\ f$ defines its domain.

In this thesis there are long formulas and vectors, with the need to go to the next row more than once, for this reason the symbol "$\hookleftarrow$" at the end of these has been used.

2.2. Definitions

Definition 2.2.1. *(Convex function). A function $f : \mathbb{R}^n \to \mathbb{R}$ is convex if* $\textbf{dom}\ f$ *is a convex set and for any x_1, $x_2 \in$* $\textbf{dom}\ f$ *and any ξ such that $0 \leq \xi \leq 1$, the following equation holds:*

$$f(\xi x_1 + (1-\xi)x_2) \leq \xi f(x_1) + (1-\xi)f(x_2). \tag{2.1}$$

If $-f$ is convex, then f is concave.

Definition 2.2.2. *(Affine function). A function $\boldsymbol{f} : \mathbb{R}^n \to \mathbb{R}^m$ is affine if it is of the form $\boldsymbol{f}(\boldsymbol{x}) = \boldsymbol{G}\boldsymbol{x} + \boldsymbol{b}$, with $\boldsymbol{G} \in \mathbb{R}^{m\times n}$ and $\boldsymbol{b} \in \mathbb{R}^m$. All affine functions are both convex and concave.*

Definition 2.2.3. *(Quadratic function). A function $f : \mathbb{R}^n \to \mathbb{R}$ is quadratic* *if it can be written in the form:*

$$f(x) : \frac{1}{2}\boldsymbol{x}^T \boldsymbol{H} \boldsymbol{x} + \boldsymbol{h}^T \boldsymbol{x} + k \tag{2.2}$$

with $\boldsymbol{H} \in \mathbb{R}^{n \times n}$ *a symmetric matrix,* $\boldsymbol{h} \in \mathbb{R}^n$ *and* $k \in \mathbb{R}$*. A quadratic function is convex if and only if* $\boldsymbol{H} \geq 0$*. In the rest of the thesis* $k = 0$ *holds, therefore the constant term* k *will be omitted.*

Definition 2.2.4. *(Convex optimisation). A convex optimisation problem is of the form*

$$\begin{aligned} \min_{x} \quad & f_0(x) \\ s.t. \quad & f_i(x) \leq b_i \quad i = 1, \ldots, m, \end{aligned} \tag{2.3}$$

where $f_0, \ldots, f_m : \mathbb{R}^n \to \mathbb{R}$ *are convex functions.*

Definition 2.2.5. *(Quadratic programming). A quadratic programming (QP) problem minimises a convex quadratic function over a polyhedron. A QP problem can be written in the following form:*

$$\begin{aligned} \min_{\boldsymbol{x}} \quad & \frac{1}{2}\boldsymbol{x}^T \boldsymbol{H} \boldsymbol{x} + \boldsymbol{h}^T \boldsymbol{x} \\ s.t. \quad & \boldsymbol{G}\boldsymbol{x} \leq \boldsymbol{b} \\ & \boldsymbol{G_e}\boldsymbol{x} = \boldsymbol{b_e} \end{aligned} \tag{2.4}$$

where $\boldsymbol{H} \in \mathbb{R}^{n \times n}$ *is symmetric,* $\boldsymbol{H} \geq 0$*,* $\boldsymbol{h} \in \mathbb{R}^n$*,* $\boldsymbol{G} \in \mathbb{R}^{m \times n}$*,* $\boldsymbol{b} \in \mathbb{R}^m$*,* $\boldsymbol{G_e} \in \mathbb{R}^{m_e \times n}$ *and* $\boldsymbol{b_e} \in \mathbb{R}^{m_e}$*.*

Definition 2.2.6. *(Clarke, forward and inverse transformation). The Clarke transformation is expressed by the following:*

$$x_\alpha = x_a \tag{2.5}$$

$$x_\beta = \frac{1}{\sqrt{3}}(x_a + 2x_b), \qquad \textit{with} \quad x \in \{i, v\}. \tag{2.6}$$

The three-phase quantities are projected from the three-phase of the reference frame to the two-axis of the orthogonal stationary reference frame by using Clarke transformation. These relationships are valid both if the three-phases system is balanced, namely, $x_a + x_b + x_c = 0$*, and if* x_α *is superposed to* x_a*, as shown in Fig. 2.1.*

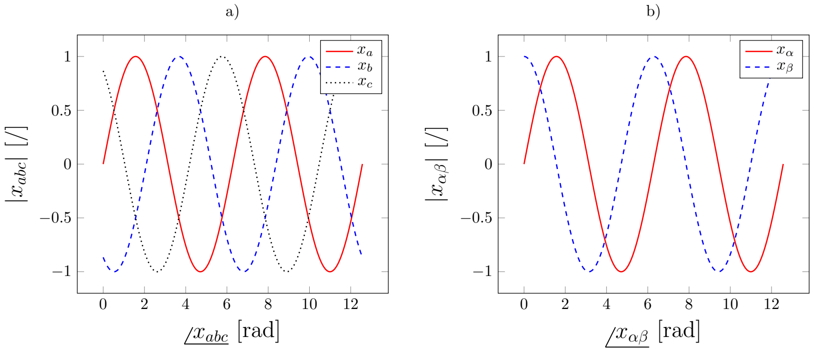

Figure 2.1.: a)Balanced three-phase system; b)Transformation of three-phase system into two-phase orthogonal one.

Otherwise the generalised Clarke transformation is described by:

$$\begin{aligned} x_\alpha &= \frac{2}{3}x_a - \frac{1}{3}(x_b + x_c) \\ x_\beta &= \frac{2}{\sqrt{3}}(x_b - x_c), \qquad \textit{with} \quad x \in \{i,\, v\}. \\ x_0 &= \frac{2}{3}\,(x_a + x_b + x_c) \end{aligned}$$

The transformation from a two-axis orthogonal stationary reference frame to a three-phase stationary reference frame is performed by using inverse Clarke. It expressed by the following equations:

$$\begin{aligned} x_a &= x_\alpha \\ x_b &= \frac{-x_\alpha + \sqrt{3}x_\beta}{2} \\ x_c &= \frac{-x_\alpha - \sqrt{3}x_\beta}{2}, \qquad \textit{with} \quad x \in \{i,\, v\}. \end{aligned}$$

Definition 2.2.7. *(Park, forward and inverse transformation). The two-axis orthogonal stationary reference frame quantities are transformed into rotating reference frame quantities using Park transformation. The transformation is expressed by the following equations:*

$$\begin{aligned} x_d &= x_\alpha \cos(\theta) + x_\beta \sin(\theta) \\ x_q &= x_\beta \cos(\theta) - x_\alpha \sin(\theta), \qquad \textit{with} \quad x \in \{i,\, v\}. \end{aligned}$$

While, the inverse Park transformation is described by:

$$\begin{aligned} x_\alpha &= x_d\cos(\theta) - x_q\sin(\theta) \\ x_\beta &= x_q\cos(\theta) + x_d\sin(\theta), \qquad \textit{with} \quad x \in \{i,\, v\}. \end{aligned}$$

Definition 2.2.8. *(The customised* $\operatorname{sgn}_\epsilon(\cdot)$*). For* $\epsilon > 0$ *arbitrarily small, let define the following continuously differentiable approximation of sign*(z)*:*

$$\operatorname{sgn}_\epsilon(z) = \begin{cases} \operatorname{sgn}(z) & |z| \geq \epsilon \\ \frac{2\epsilon - |z|}{\epsilon^2} z & |z| \in (\epsilon/2, \epsilon) \\ \dfrac{3z}{2\epsilon} & |z| \leq \epsilon/2. \end{cases} \tag{2.7}$$

Accordingly, the derivative is given by

$$\chi_\epsilon(z) = \begin{cases} 0 & |z| \geq \epsilon \\ \dfrac{2(\epsilon - |z|)}{\epsilon^2} & |z| \in (\epsilon/2, \epsilon) \\ \dfrac{3}{2\epsilon} & |z| \leq \epsilon/2. \end{cases} \tag{2.8}$$

Moreover, for a function $f(t)$*, the first and second left derivative operators* $D^- f(t)$ *and* $D^{-,2} f(t)$ *are defined as follows:*

$$D^- f(t) \overset{\text{def}}{=} \lim_{h \to 0} \frac{f(t) - f(t - |h|)}{|h|}, \tag{2.9}$$

$$D^{2,-} f(t) \overset{\text{def}}{=} \lim_{h \to 0} \frac{f(t) - 2f(t - |h|) + f(t - 2|h|)}{|h|^2}. \tag{2.10}$$

2.3. Remarks

Remark 2.3.1. *It should be noted that, for control implementation purposes, the left-derivative* $D^-\theta_e(t)$ *can be replaced by a discrete derivative defined by the incremental ratio*

$$D_\delta^- \theta_e(t) \overset{\text{def}}{=} \frac{\theta_e(t) - \theta_e(t - \delta)}{\delta} \quad \textit{for} \quad \delta > 0 \quad \textit{sufficiently small.}$$

In a similar way one can discretise the second derivative:

$$D_\delta^{2,-} \theta_e(t) \overset{\text{def}}{=} \frac{\theta_e(t) - 2\theta_e(t - \delta) + \theta_e(t - 2\delta)}{\delta^2}.$$

2.4. Theorems

Theorem 2.4.1. *(Bézout's Theorem). Let* $\mathcal{C}_i$*,* $i = 1, ..., n$*, be algebraic manifolds embedded in the* n*-dimensional space, having no common components. Let assume that the degree of* $\mathcal{C}_i$ *is* $d_i \geq 1$*. Then the number* ϖ *of intersection points (possibly complex, and counted with multiplicity) between the manifolds* $\mathcal{C}_i$ *is finite and it is given by* $\varpi = d_1 \cdot d_2 \cdots d_n$*.*

Part I.

White-Box Approach

Chapter 3.

Introduction

As well known, advanced control applications in electrical drives require feedback information about rotor positions and, when speed tracking is required, also rotor speed. Nonetheless, by the adoption of sensorless approaches, speed and/or position sensors could be substituted by mathematical algorithms, also because in some compact design, there is no extra installation space for sensors [2]. Costs are this way reduced exploiting low-cost motor drives (this is especially the case of Permanent Magnet Synchronous Motors (PMSMs), which are becoming very popular), and sensors inaccuracies and/or faults due to malfunctioning of sensing devices are avoided [11]. For these purposes, a widely used control technique is the so called Field Oriented Control (FOC), consisting in closed loop current control. Sensorless techniques could be classified based on the operational domain [12]. In surface PMSMs, whose low-speed performances are poor, back-Electro-Motive Force (bEMF) based approaches are very frequent [11,13]. The main drawback is that observability property is lost at zero speed [14], given the induced voltage vanishing at low speed [11]. At low-speed, non-model-based techniques founded on rotor saliency are typically used, realised with a high frequency signal injection [13, 15]. However, injected high-frequency (HF) signals can produce more losses and larger torque ripple [2], bringing also high-frequency noise, at frequencies higher that the bandwidth of the regulators [16]. Whole speed range sensorless operation can be achieved by combining machine anisotropy based methods with machine model based methods [17]. However, a hybrid sensorless control system will increase complexity of the system. In order to properly handle such limitations, observers have been adopted in the literature. An adaptive interconnected scheme has been proposed in [15], while an extended Kalman Filter approach has been exploited in [18], this latter requiring intensive computing. Pursuing easy implementability, robustness and good dynamic behaviour, sliding mode observers are being currently largely employed [19, 20]. In addition, nonlinear back-EMF-based observers for rotor position estimation have been recently developed [11, 21–24].

In most of the cited cases, the need of theoretically proving closed-loop convergence often induces the introduction of strong assumptions which are rarely verified in practice. Just as an example, the initial angular rotor position is often assumed known (eventually with a bounded uncertainty), but experimental practice shows that this is hardly the case with real devices. Starting the drive from unknown initial position is challenging for loads whose torque is constant and independent of speed or that needs high starting torque. In this case it may be necessary to assist a sensorless technique with even a low resolution sensor like hall effect to bring it to a minimum rotational speed at which the observer converges and provides reliable position and speed information [25]. In [26] a preliminary alignment procedure is performed with the aim of adhering to the local nature of the presented results.

On the other hand, several and heterogeneous approaches to the identification problem of the motor model parameters have been proposed in the past decade [27–31]. All the mentioned results require direct measurements of motor angular position and speed, this making the methods highly sensitive to sensors inaccuracies and/or faults (of course the presence of dedicated sensors is mandatory). However, the problem of designing a feedback control - with rigorous stability proof - which guarantees the position/speed tracking for sensorless PMSMs with simultaneous estimation of the uncertain load torque and stator resistance is still open. Even recent papers addressing the position/speed estimation problem either require the knowledge of stator resistance [32] or rely on the rotor speed measurements to achieve asymptotic estimation [33,34]. In this more challenging framework of sensorless PMSMs, fewer results are available. In particular, online identification of stator resistance is achieved in [35] by means of a sensorless decoupling controller. An online stator resistance estimation method is proposed in [36], by injecting current into the d-axis, the stator resistance is estimated with high accuracy, but the effect of injected current on drive system is ignored. In [37], the stator resistance is estimated only at steady state based on the addition of rotor position offsets and neural network. Furthermore, a neural network is not easy to be implemented on a microprocessor. In [2], an online stator resistance estimation scheme is proposed based on a modified first-order sliding mode observer. Stable conditions of the observer have been obtained but a non-robust PI-based control solution has been used for the FOC of the PMSM. Moreover, the speed has been estimated by a low pass filter, causing gain attenuation and phase delay [38]. A nonlinear observer for motors operating in quasi steady-state conditions is proposed instead in [39], using integral adaptation laws and signal injection. Adaptive estimators with quadratic stability guarantees have been used in [40] for linear models of PMSMs. The nonlinear nature of the system and the additional challenges caused by the sensorless setup pose however a number of limitations and/or constraints reducing the successful applicability of adaptive parameter estimators for PMSMs in practice. In [26] the local exponential stability of the origin of the overall closed loop error system guarantees certain robustness properties, though restricted to sufficiently small uniformly bounded perturbations, and relatively small initial tracking and estimation errors. A possible strategy to overcome the problems described above has been presented in [41–43]. A further improvement and strengthening of such techniques is proposed in the present note, where a sensorless, back-EMF based, FOC algorithm is designed, featuring robustness with respect to motor parameters variation.

3.1. Problem statement

The main features of the proposed strategy can be summarised as follows:

(P.1) On-line computation of the model parameter and of the *initial angular position*.

(P.2) Rotor *angular position estimation* using electrical signal.

(P.3) *Sensorless* speed reference tracking.

(P.4) *Robustness* to bounded parameter variations affecting the electrical and mechanical system.

(P.5) Algorithm *optimization* for the implementation on a Digital Signal Processing (DSP) board.

The availability of a reliable identification method, theoretically proved, for motor parameters and angular initial condition, implementable on a DSP board has allowed us to propose a fully sensorless, embedded control strategy for PMSM speed tracking control. In addition, the experimental testing of the overall sensorless control scheme is here provided, proving the effectiveness of the proposed approach. The major added value of the method proposed in this thesis is to provide a fully sensorless scheme for the simultaneous estimation of initial angular position and motor parameters, such as stator resistance and/or inductance, with the additional feature of being usable with any desired sensorless control technique for the nonlinear PMSM model.

Chapter 4.

Permanent Magnet Synchronous Motor

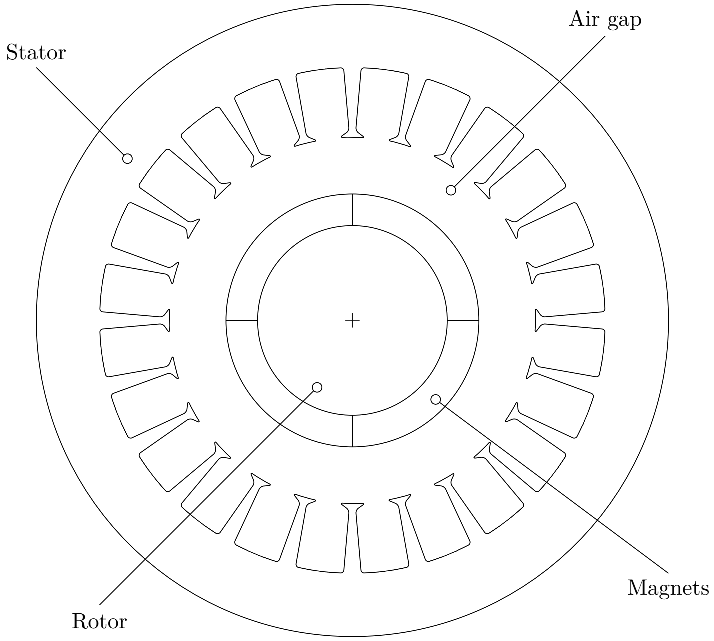

Figure 4.1.: PMSM cross section.

Permanent magnet synchronous motors, also known in the literature as sinusoidal brushless motors, are increasingly used in industry, especially in small and medium power servo drives. The employed electromechanical conversion follows the operating principle of the electrodynamic systems. It is based on the interaction between conductors crossed by currents and magnetic fields created by permanent magnets. Through the electromagnetic phenomena, it achieves the electro-mechanical power conversion, which naturally can operate in both conversion directions (from the electric system to the mechanical one and vice versa). In the condition in which the external electric energy is used to generate mechanical energy, we speak of functioning as a motor; otherwise, we will talk about a generator. In cases such as this work, in which the machine is used mainly for the generation of movement, it is classified as a motor, although the transfer of power may in some moments take place from the mechanical system to the electric one, *e.g.* in deceleration. The engine consists of two coaxial parts joined together by a rotoidal joint [44]. The fixed part to the environment, generally chosen as an external reference, is called stator in which are placed the windings. While the other one is called rotor which is subject to the torque generated and connected to the mechanism to be moved and in which are placed the permanent magnets; both parts are separated by the air gap as Fig. 4.1 is depicted. Whilst in the mathematical speaking, the engine can be considered as a feedback interconnection between the dynamic, *i.e.* electrical and mechanical systems, as illustrated in Fig. 4.2.

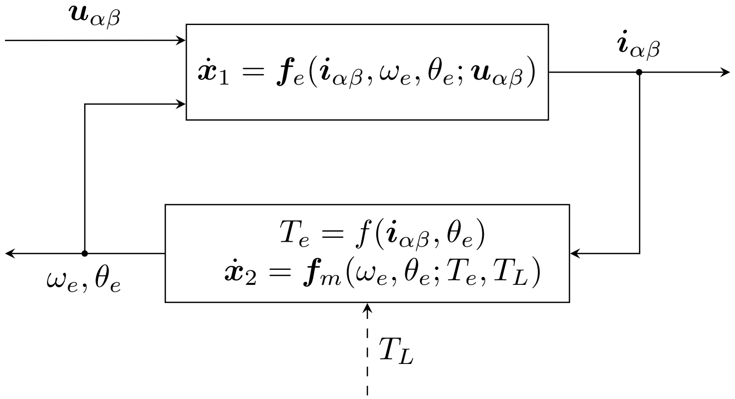
$\boldsymbol{u}_{\alpha\beta}$
$\dot{\boldsymbol{x}}_1 = \boldsymbol{f}_e(\boldsymbol{i}_{\alpha\beta}, \omega_e, \theta_e; \boldsymbol{u}_{\alpha\beta})$
$\boldsymbol{i}_{\alpha\beta}$
$T_e = f(\boldsymbol{i}_{\alpha\beta}, \theta_e)$
$\dot{\boldsymbol{x}}_2 = \boldsymbol{f}_m(\omega_e, \theta_e; T_e, T_L)$
ω_e, θ_e
T_L

Figure 4.2.: The interconnection between the mechanic and electric dynamics.

4.1. Electrical subsystem

4.1.1. The three-phase model, "*abc*" reference frame

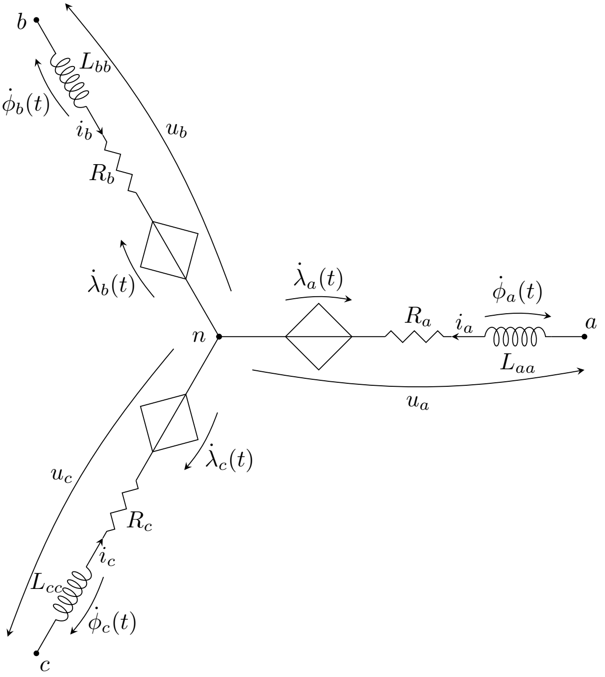

Figure 4.3.: The equivalent circuit of the stator.

To describe the functioning of the brushless motor it is useful to start from the KVL to its phases a, b, c, as shown in Fig. 4.3, following the PSC[1] convention:

$$\boldsymbol{u}(t) = R\boldsymbol{i}(t) + \dot{\boldsymbol{\psi}}(t) \tag{4.1}$$

where $\boldsymbol{u}(t) \in \mathbb{R}^3$ is the vector of the stator voltages, $R \in \mathbb{R}^+$ is the phase resistance, $\boldsymbol{i}(t) \in \mathbb{R}^3$ is the vector of the stator currents and $\boldsymbol{\psi}(t) \in \mathbb{R}^3$ is the vector of the stator linkage fluxes. If the hypothesis about the absence of saturation of the magnetic circuits holds, the flux vector can be described by:

$$\boldsymbol{\psi}(t) = \boldsymbol{\lambda}(t) + \boldsymbol{\phi}(t). \tag{4.2}$$

In detail, (4.2) represents the sum of the permanent magnet flux linkage denoted by $\boldsymbol{\lambda}(t) \in \mathbb{R}^3$ and the flux generated by the phase currents denoted by

---

[1] In electrical engineering, the Passive Sign Convention is a standard rule adopted universally by the electrical engineering community for defining the sign of electric power. In this specific case the loader absorbs the electric power.

$\boldsymbol{\phi}(t) \in \mathbb{R}^3$, for each phase:

$$\boldsymbol{\lambda}(t) = \lambda_{PM} e^{\iota(Np\theta_m + h\pi)} \qquad \text{with} \qquad h \in \left\{0, \frac{2}{3}, -\frac{2}{3}\right\} \tag{4.3}$$

and

$$\boldsymbol{\phi}(t) = L_{ss}\boldsymbol{i}(t) - |L_{ms}|\boldsymbol{P}\boldsymbol{i}(t) \qquad \text{with} \qquad \boldsymbol{P} \overset{\text{def}}{=} \begin{bmatrix} 0 & 1 & 1 \\ 1 & 0 & 1 \\ 1 & 1 & 0 \end{bmatrix}; \tag{4.4}$$

if the hypothesis of magnetic isotropy and the phase windings symmetry are held.

The introduced electrical subsystem is a natural consequence obtained following the physics laws that govern the process, despite from a control point of view the use of these equations is not a smart choice.

$$\text{KCL:} \sum_{h\in\{a,b,c\}} i_h(t) = 0 \qquad\qquad \text{KVL:} \sum_{h\in\{a,b,c\}} u_h(t) = 0 \tag{4.5}$$

If the above conditions hold[2], it is possible to reduce the three-phase electric model formulation to two dimensions, as it is convenient for modelling as well as for the control. Usually, two orthogonal axis systems are used, one is integral with the stator (so-called Clarke transformation, carried out by the projection matrix), and the other with the rotor (so-called Park transformation, carried out by the rotation matrix).

4.1.2. Reduced model, "$\alpha\beta$" reference frame

Applying the projection matrix, Clark transformation, the model described by (4.1) becomes:

$$L\frac{d}{dt}\boldsymbol{i}_{\alpha\beta}(t) = -\frac{R}{L}\boldsymbol{i}_{\alpha\beta}(t) - \frac{\psi}{L}\mathbf{R}^T(\theta_e(t))\boldsymbol{\Gamma}\omega_e(t) + \frac{1}{L}\boldsymbol{u}_{\alpha\beta}(t). \tag{4.6}$$

$$\begin{gathered} \boldsymbol{i}_{\alpha\beta}(t) \in \mathscr{X}_1 \simeq \mathbb{R}^2, \quad \boldsymbol{u}_{\alpha\beta}(t) \in \mathscr{U} \simeq \mathbb{R}^2, \quad R, L, \psi \in \mathscr{P}_1 \simeq \mathbb{R}^+, \\ \boldsymbol{\Gamma} \overset{\text{def}}{=} \begin{bmatrix} 0 \\ 1 \end{bmatrix}, \quad \mathbf{R}(\cdot) \overset{\text{def}}{=} \begin{bmatrix} \cos(\cdot) & \sin(\cdot) \\ -\sin(\cdot) & \cos(\cdot) \end{bmatrix}, \end{gathered} \tag{4.7}$$

where $\boldsymbol{i}_{\alpha\beta}(t)$ and $\boldsymbol{u}_{\alpha\beta}(t)$ are the equivalent stator vectors of the current and voltage, respectively. Parameters like the resistance, the inductance and flux linkage, previously reported, do not change using the transformation. $\theta_e(t)$ and $\omega_e(t)$ will be introduced in section 4.2, while $\mathbf{\Gamma}$ and $\mathbf{R}$ defined as in (4.7) are employed to obtain a compact matrix formulation. The advantages of these transformed dynamic are the dimension's reduction, $[a, b, c] \to [\alpha, \beta]$, consequently a minor number of the controllers. However, the benefit is the decoupling of the mutual inductance.

---

[2] Usually, these two conditions are always satisfied because the electric motor is a balanced three-phase load. So in a possible availability of the neutral conductor, its current is equal to zero.

4.1.3. Reduced model, "dq" reference frame

The next and last step that simplify the model described by (4.6) is obtained applying the Park transformation, generating the following matrix relationship:

$$\frac{d}{dt}\boldsymbol{i}_{dq}(t) = -\frac{R}{L}\boldsymbol{i}_{dq}(t) - \omega_e(t)\left[\boldsymbol{\Upsilon}\boldsymbol{i}_{dq}(t) + \frac{\psi}{L}\mathbf{\Gamma}\right] + \frac{1}{L}\boldsymbol{u}_{dq}(t). \tag{4.8}$$

$$\begin{gathered}\boldsymbol{i}_{dq}(t) \in \mathscr{X}_1 \simeq \mathbb{R}^2, \quad \boldsymbol{u}_{dq}(t) \in \mathscr{U} \simeq \mathbb{R}^2, \quad R, L, \psi \in \mathscr{P}_1 \simeq \mathbb{R}^+, \\ \mathbf{\Gamma} \overset{\text{def}}{=} \begin{bmatrix} 0 \\ 1 \end{bmatrix}, \quad \boldsymbol{\Upsilon} \overset{\text{def}}{=} \begin{bmatrix} 0 & -1 \\ 1 & 0 \end{bmatrix},\end{gathered} \tag{4.9}$$

where $\boldsymbol{i}_{dq}(t)$ and $\boldsymbol{u}_{dq}(t)$ are the equivalent stator vectors of the current and voltage, respectively. Parameters like the resistance, the inductance and flux linkage, previously reported, do not change using the transformation. $\theta_e(t)$ and $\omega_e(t)$ will be introduced in section 4.2, while $\mathbf{\Gamma}$ and $\boldsymbol{\Upsilon}$ defined as in (4.9) are used to obtain a compact matrix formulation. The employment of the transformed dynamic (4.8) entails the decoupling of the contributions generated by currents $i_d(t)$ and $i_q(t)$. Thuse, it makes the motor like a DC motor. The electrical quantities change from sinusoidal to continuous trends at steady state.

4.2. Mechanical subsystem

So far, the electric dynamic has been well described. However, we must bear in mind that the electric motor relates electrical and mechanical quantities. The junction between the two subsystems is made by the electric torque described by algebric relationship (4.10). It represents the output for the electric dynamic and input for the mechanical dynamic. If we therefore also consider the mechanical equations, the following relationships must also be respected:

$$T_e(t) = \frac{3}{2} N_p \psi i_q(t) \equiv \frac{3}{2} N_p \psi \left[i_\beta(t) \cos(\theta) - i_\alpha(t) \sin(\theta) \right]. \tag{4.10}$$

$$\frac{d}{dt}\omega_e(t) = -\frac{B}{J}\omega_e(t) + \frac{N_p}{J}\left[T_e(\boldsymbol{i}_{\alpha\beta}, \theta_e) - T_L(t)\right] \tag{4.11}$$

$$\frac{d}{dt}\theta_e(t) = \omega_e(t), \tag{4.12}$$

$$\omega_e(t), \theta_e(t) \in \mathscr{X}_2 \simeq \mathbb{R}, \quad T_L(t) \in \mathscr{D} \simeq \mathbb{R}, \quad B, J \in \mathscr{P}_2 \simeq \mathbb{R}^+,$$
$$N_p \in \mathscr{P}_3 \simeq \mathbb{N}^+, \quad Te(\cdot,\cdot) : \mathbb{R}^2 \times \mathbb{R} \to \mathbb{R}.$$

Equations (4.11) and (4.12) describe how the electromechanical energy conversion occurs, where $\omega_e(t)$ and $\theta_e(t)$ are the velocity and the angular position of the rotor; $T_e(t)$ and $T_L(t)$ are the electric and load torques, while J and B identify the rotor inertia and its viscous coefficient. The constant N_p is the number of pole pairs. At this stage, the mathematical model that describes the introduced physical process is well defined.

4.3. Assumptions

Let introduce the following assumptions:

(A.1) The parameter B and the load torque $T_L(t)$ are uncertain, with bounded uncertainties:

$$\begin{aligned} B &= \bar{B} + \Delta B, & |\Delta B| &\leq \rho_B; \\ T_L(t) &= \bar{T}_L + \Delta T_L(t), & |\Delta T_L(t)| &\leq \rho_{T_L}; \end{aligned} \tag{4.13}$$

(A.2) The motor resistor is assumed uncertain, with bounded uncertainty. Parameter variations slowly varying with respect to the motor dynamics [15] have been considered:

$$R = \bar{R} + \Delta R, \quad \dot{R} \simeq 0, \quad -\bar{R} < \underline{\rho}_{\Delta R} \leq \Delta R \leq \overline{\rho}_{\Delta R} \tag{4.14}$$

being $\bar{R}$ the nominal values and ΔR the corresponding uncertainty, assumed bounded by the known constants $\underline{\rho}_{\Delta R}$, $\overline{\rho}_{\Delta R}$.

(A.3) The absolute value of the rotor velocity $\omega_e(t)$ is bounded by a known constant, due to physical constraints:

$$|\omega_e(t)| \leq \omega_e^M. \tag{4.15}$$

(A.4) The measurable signals are only $i_\alpha(t)$ and $i_\beta(t)$.

(A.1) is a classical needed assumption for ensuring the robust achievement of a sliding motion. In order to simplify the mathematical development, parameters J and L have been assumed known. Nonetheless, the presented approach can be extended to cope with bounded variation of J and L.

(A.2) is necessary for two reasons: i) Since the algorithm acquires $u_{\alpha,\beta}$ and $i_{\alpha,\beta}$ during three different time instants $t1 < t2 < t3$, R should not vary in $[t1, t3]$; ii) ΔR is the resistance variation of R therefore the lower bound $\underline{\rho}_R$ cannot be less than $-\bar{R}$, where $\bar{R}$ is the nominal value.

(A.3) is useful during control design when the worst case has been taken into account.

(A.4) corresponds to the usual scenario for all controllers type, *i.e.* sensored and sensorless.

Chapter 5.

On-line Determination of (θ_0, ΔR) and Control Design

5.1. The unknowns (θ_0, ΔR)

In this chapter an analytical method, holding under weak conditions, is presented for the identification of the resistor variation ΔR in (4.6) and of the rotor initial angular position $\theta_e(0) = \theta_0$ from current measurements. No injection of auxiliary signals is required. The key idea is to analytically solve a set of polynomial equations, obtained rearranging the motor equations coupled with an observer. Only a few currents samples are needed to achieve the rank requirement needed for the solution of the equations set, so that the identification procedure can be repeated with arbitrary frequency. A set of polynomial equations is derived from the output of the electrical subsystem and solved with respect to ΔR and θ_0. Introduce the following pseudo-observers for $i_\alpha(t)$ and $i_\beta(t)$:

$$\begin{cases} \dfrac{d\hat{i}_\alpha(t)}{dt} = -\dfrac{\bar{R}}{L} i_\alpha(t) + \dfrac{1}{L} u_\alpha(t) \\ \dfrac{d\hat{i}_\beta(t)}{dt} = -\dfrac{\bar{R}}{L} i_\beta(t) + \dfrac{1}{L} u_\beta(t) \end{cases} \tag{5.1}$$

and define the errors:

$$e_\alpha(t) = i_\alpha(t) - \hat{i}_\alpha(t) \tag{5.2}$$

$$e_\beta(t) = i_\beta(t) - \hat{i}_\beta(t). \tag{5.3}$$

From (4.6) and (5.1), the dynamics of $e_\alpha(t)$ and $e_\beta(t)$ are obtained as follow:

$$\begin{gathered}\dot{e}_\alpha(t) = \frac{d}{dt} i_\alpha(t) - \frac{d}{dt}\hat{i}_\alpha(t) = \\ = -\frac{R}{L} i_\alpha(t) + \omega_e(t)\frac{\lambda_0}{L}\sin(\theta_e(t)) + \frac{1}{L}v_\alpha(t) - \left(-\frac{\bar{R}}{L} i_\alpha(t) + \frac{1}{L}v_\alpha(t)\right) = \\ = -\frac{\bar{R}+\Delta R}{L} i_\alpha(t) + \omega_e(t)\frac{\lambda_0}{L}\sin(\theta_e(t)) + \frac{1}{L}v_\alpha(t) - \left(-\frac{\bar{R}}{L} i_\alpha(t) + \frac{1}{L}v_\alpha(t)\right) = \\ = -\frac{\Delta R}{L} i_\alpha(t) + \omega_e(t)\frac{\lambda_0}{L}\sin(\theta_e(t)),\end{gathered}$$

the same steps are valid also for $\dot{e}_\beta(t)$.

$$\begin{cases} \dot{e}_\alpha(t) = -\dfrac{\Delta R}{L} i_\alpha(t) + \omega_e(t)\dfrac{\psi}{L}\sin\theta_e(t) \\ \dot{e}_\beta(t) = -\dfrac{\Delta R}{L} i_\beta(t) - \omega_e(t)\dfrac{\psi}{L}\cos\theta_e(t) \end{cases} \tag{5.4}$$

Variables $e_\alpha(t)$ and $e_\beta(t)$ are initialized to zero, setting

$$\hat{i}_\alpha(0) = i_\alpha(0) \quad \text{and} \quad \hat{i}_\beta(0) = i_\beta(0),$$

and correspond to the contributions of the unknown terms in the electrical equations. The following additional integral states I_α, I_β can be introduced:

$$I_\alpha(t) = \int_0^t i_\alpha(\tau)d\tau, \quad I_\beta(t) = \int_0^t i_\beta(\tau)d\tau,$$

Integrating equations (5.4), one has:

$$\begin{aligned} e_\alpha(t) &= -\frac{\Delta R}{L} I_\alpha - \frac{\psi}{L}\left(\cos(\theta_e(t)) - \cos(\theta_0)\right) \\ e_\beta(t) &= -\frac{\Delta R}{L} I_\beta - \frac{\psi}{L}\left(\sin(\theta_e(t)) - \sin(\theta_0)\right) \end{aligned}$$

or equivalently

$$\begin{aligned} e_\alpha(t) + \frac{\Delta R}{L} I_\alpha(t) - \frac{\psi}{L}\cos\theta_0 &= -\frac{\psi}{L}\cos\theta_e(t); \\ e_\beta(t) + \frac{\Delta R}{L} I_\beta(t) - \frac{\psi}{L}\sin\theta_0 &= -\frac{\psi}{L}\sin\theta_e(t). \end{aligned} \tag{5.5}$$

Taking the sum of the squares yields the identity:

$$\begin{aligned}&\left(e_\alpha(t) + \frac{\Delta R}{L} I_\alpha(t) - \frac{\psi}{L}\cos\theta_0\right)^2 + \hookleftarrow\\ &+\left(e_\beta(t) + \frac{\Delta R}{L} I_\beta(t) - \frac{\psi}{L}\sin\theta_0\right)^2 = \frac{\psi^2}{L^2}.\end{aligned} \tag{5.6}$$

As the time t varies, (5.6) constitutes an infinite family of equations with unknown variables $\theta_0, \Delta R$. Exploiting the left-hand side, equation (5.6) can be rearranged as:

$$\begin{aligned}&\mathbf{W}(t) \cdot [\Delta R^2, \quad \Delta R, \quad \Delta R\cos\theta_0, \hookleftarrow\\ &\qquad \Delta R\sin\theta_0, \quad \cos\theta_0, \quad \sin\theta_0]^T + E(t) = 0\end{aligned}$$

with:

$$\begin{aligned}\mathbf{W}(t) \overset{\text{def}}{=} \Bigg[&\frac{I_\alpha^2(t) + I_\beta^2(t)}{L^2}, \frac{2\left(e_\alpha(t)I_\alpha(t) + e_\beta(t)I_\beta(t)\right)}{L}, \frac{-2\psi}{L^2} I_\alpha(t), \hookleftarrow\\ &\frac{-2\psi}{L^2} I_\beta(t), \frac{-2\psi}{L} e_\alpha(t), \frac{-2\psi}{L} e_\beta(t)\Bigg]\end{aligned} \tag{5.7}$$

$$E(t) \overset{\text{def}}{=} e_\alpha^2(t) + e_\beta^2(t).$$

The following result holds:

Theorem 5.1.1. *Consider two distinct time instants t_1, t_2 such that the vector of coefficients $\mathbf{W}(t_2)$ is not a multiple of $\mathbf{W}(t_1)$. The triple $(\cos\theta_0, \sin\theta_0, \Delta R) = (x, y, z)$ satisfies the following set of quadratic equations in the variables (x, y, z)*

$$\begin{cases} x^2 + y^2 = 1; \\ \mathbf{W}(t_1) \cdot [z^2 \quad z \quad zx \quad zy \quad x \quad y]^T + E(t_1) = 0; \\ \mathbf{W}(t_2) \cdot [z^2 \quad z \quad zx \quad zy \quad x \quad y]^T + E(t_2) = 0, \end{cases} \tag{5.8}$$

which admits a finite number of solutions. If there exists an additional time instant t_3 such that condition

$$rank\begin{bmatrix} \mathbf{W}(t_1) & \mathbf{W}(t_2) & \mathbf{W}(t_3) \end{bmatrix}^T = 3 \tag{5.9}$$

is fulfilled, then considering the equation

$$\mathbf{W}(t_3) \cdot [z^2 \quad z \quad zx \quad zy \quad x \quad y]^T + E(t_3) = 0, \tag{5.10}$$

two cases are admissible:

i) the triple $(\cos\theta_0, \sin\theta_0, \Delta R)$ is the unique solution of equations (5.8), (5.10);

ii) the polynomial system (5.8), (5.10) admits $1 < \nu \leq 4$ *solutions.*

Proof. By Bézout's theorem [45], the system (5.8) admits at most $8 = 2^3$ distinct solutions. On the other hand, for any $t \geq 0$, the equation $\mathbf{W}(t) \cdot [z^2 \quad z \quad zx \quad zy \quad x \quad y]^T = -E(t)$ can be rewritten in the equivalent form $z^2 = zg(t,x,y) + h(t,x,y)$, where $g(\cdot,x,y)$, $h(\cdot,x,y)$ are polynomial functions obtained from the coefficients of $\mathbf{W}(t)$ and $E(t)$. Therefore the system (5.8), (5.10) is equivalent to

$$\begin{cases} x^2 + y^2 = 1 \\ \frac{h(t_1,x,y)-h(t_2,x,y)}{g(t_2,x,y)-g(t_1,x,y)} = \frac{h(t_1,x,y)-h(t_3,x,y)}{g(t_3,x,y)-g(t_1,x,y)} \\ z(g(t_2,x,y)-g(t_1,x,y)) = h(t_1,x,y)-h(t_2,x,y) \\ z^2 = zg(t_1,x,y)+h(t_1,x,y) \end{cases} \tag{5.11}$$

The first two equations are quadratic and depending only on the variables x, y; as a consequence, applying again Bézout's theorem and observing that z is completely determined by the third equation, the maximum number of admissible solutions is $4 = 2^2$. It should be pointed out that the second equation in (5.11) is well-posed if and only if (5.9) is fulfilled. □

5.1.1. Multiple solutions: a decision algorithm

Consider the case when the previously described algebraic method fails in isolating the true solution, and suppose that system (5.11) (or system (5.8)) admits $1 < \nu \leq 4$ ($1 < \nu \leq 8$) distinct solutions (X_k, Y_k, Z_k), $k = 1, ..., \nu$. An approach based on multiple models can be used for building a decision algorithm, as described in the following. Consider the following set of ν copies of the pseudo-observer (5.1), each associated to an admissible triple (X_k, Y_k, Z_k), $k = 1, ..., \nu$

$$\begin{cases} \dfrac{d\eta_\alpha^{(k)}(t)}{dt} = -\dfrac{\bar{R} + Z_k}{L} i_\alpha(t) + \dfrac{1}{L} u_\alpha(t) \\ \dfrac{d\eta_\beta^{(k)}(t)}{dt} = -\dfrac{\bar{R} + Z_k}{L} i_\beta(t) + \dfrac{1}{L} u_\beta(t). \end{cases} \qquad k = 1, ..., \nu$$

Writing the dynamics of $e_\alpha^{(k)}(t) = i_\alpha(t) - \eta_\alpha^{(k)}(t)$, $e_\beta^{(k)}(t) = i_\beta(t) - \eta_\beta^{(k)}(t)$ as in (5.4), and integrating them, one gets:

$$\begin{cases} -\dfrac{L}{\psi}(i_\alpha(t) - \eta_\alpha^{(k)}(t)) - X_k \overset{\text{def}}{=} c_k(t) \\ -\dfrac{L}{\psi}(i_\beta(t) - \eta_\beta^{(k)}(t)) - Y_k \overset{\text{def}}{=} s_k(t), \end{cases} \qquad k = 1, ..., \nu \tag{5.12}$$

where there exists at least one $k^* \in \{1, ..., \nu\}$ such that:

$$\{c_{k^*}(t), s_{k^*}(t)\} = \{\cos\theta_e(t), \sin\theta_e(t)\} \qquad \forall t \geq 0.$$

Consider now ν replicas of the original plant (4.6), each associated to an admissible triple (X_k, Y_k, Z_k), $k = 1, ..., \nu$. Integrating by parts and using the expressions (5.12), the dynamical response of each copy of the plant is given by

$$\begin{cases} i_\alpha^{(k)}(t) & = e^{-\frac{(\bar{R}+Z_k)t}{L}} i_\alpha(0) + \frac{\psi}{L}\left(e^{-\frac{(\bar{R}+Z_k)t}{L}} X_k - c_k(t)\right) + \text{↵} \\ & +\psi\frac{\bar{R}+Z_k}{L^2}\int_0^t e^{-\frac{(\bar{R}+Z_k)(t-\tau)}{L}} c_k(\tau)d\tau + V_\alpha, \\ i_\beta^{(k)}(t) & = e^{-\frac{(\bar{R}+Z_k)t}{L}} i_\beta(0) + \frac{\psi}{L}\left(e^{-\frac{(\bar{R}+Z_k)t}{L}} Y_k - s_k(t)\right) + \text{↵} \\ & +\psi\frac{\bar{R}+Z_k}{L^2}\int_0^t e^{-\frac{(\bar{R}+Z_k)(t-\tau)}{L}} s_k(\tau)d\tau + V_\beta. \end{cases}$$

where V_α, V_β are the forced responses to inputs u_α, u_β. Fixing the time horizon $T > 0$ and defining the cost functional

$$\mathcal{J}(k, T) := \int_0^T ||i_\alpha(t) - i_\alpha^{(k)}(t)||^2 + ||i_\beta(t) - i_\beta^{(k)}(t)||^2 dt, \tag{5.13}$$

one gets

$$\min_{k=1,\dots,\nu} \mathcal{J}(k, T) = 0,$$

$$(\cos\theta_0, \sin\theta_0, \Delta R) = (X_{k^*}, Y_{k^*}, Z_{k^*}) \tag{5.14}$$

with

$$k^* = \arg\min_{k=1,\dots,\nu} \mathcal{J}(k, T). \tag{5.15}$$

Note that, if for any $T > 0$ the integer k^* is not unique, the triple of parameters (X_k, Y_k, Z_k) are *indistinguishable*: they provide the same effects on the system output.

Remark 5.1.1. *The development discussed so far can account also for constant uncertainties affecting the inductance parameter L, at the price of an increase of the number of feasible solutions. In particular, if both R and L are uncertain, these parameters (together with θ_0) have to satisfy a system of* 5 *quadratic equations, which is the natural extension of (5.8).*

5.1.2. Numerical solution algorithm for DSP implementation

The experimental validation of the proposed approach requires that equations (5.8), (5.10) are solved using a DSP architecture. In order to find the zeros of the non-linear function, alleviating the computational burden, the bisection method [46] has been chosen due to the particular form of formula (5.7). Indeed, though the function is transcendent with respect to θ_0, is a polynomial of degree two with respect to ΔR. Taking into account (5.8), (5.10), and recasting expression (5.7) into $f_{t_i}(\theta_0, \Delta_R)$ with $i \in \{1, 2, 3\}$, the problem can be formalised as follows:

$$\begin{cases} f_{t_1}(\theta_0, \Delta R) = 0 \\ f_{t_2}(\theta_0, \Delta R) = 0 \\ f_{t_3}(\theta_0, \Delta R) = 0 \end{cases} \tag{5.16}$$

where the first two equations can be solved with respect to ΔR in closed form. Then, exploiting the third equation, the best numerical solution $(\theta_0,\, \Delta R)$ can be found according to Fig. 5.1. When the motor starts (open-loop mode), the DSP acquires the electrical samples $(i_{\alpha,\beta},\, u_{\alpha,\beta})$ in $t_1 < t_2 < t_3$ such that (5.9) is fulfilled. Then the coefficients of (5.16) are computed. Namely, from $f_{t_1}(\theta_0, \Delta R) = 0$, two possible roots for ΔR, denoted by $f_{2,\Delta R_1}(\theta_0)$ and $f_{2,\Delta R_2}(\theta_0)$, can be found. These two roots depend on θ_0. Inserting the two expressions in f_{t_2} and applying the bisection method the four pairs of candidate solutions $(\theta_{0_1},\, \Delta R_1)$, $(\theta_{0_2},\, \Delta R_2)$, $(\theta_{0_3},\, \Delta R_3)$, $(\theta_{0_4},\, \Delta R_4)$ are obtained. An arbitrary positive constant ε has been chosen to obtain a tolerance for the algorithm stopping criterion. The best solution has been selected using the following criteria:

$$\min_{k=1,2,3,4} |f_{t_3}(\theta_{0_k}, \Delta R_k)| \quad \text{and} \quad \underline{\rho}_{\Delta R} \leq \Delta R \leq \overline{\rho}_{\Delta R}.$$

To be clearer a graphic representation of the system (5.16) is depicted in Figs. 5.2-5.5. Figures 5.2-5.3 show the scenario with nominal value. whilst, Figs. 5.4-5.5 show the case with a variation resistance of the +10% of the nominal value $\bar{R}$. If a single solution cannot be identified, the search algorithm can be further refined using the multiple-model optimisation scheme (5.15), whose computational burden is fairly low as it consists in a finite number of comparisons. Finally, in order to determine the angle $\theta_3 \overset{\text{def}}{=} \theta_e(t_3)$ to be used for the initialisation of the closed-loop controller, the DSP numerically integrates the model (4.6) using the correction parameter ΔR:

$$\theta_3 = \operatorname{arctg} \frac{-\left(i_\beta(t_3) + \frac{\bar{R}+\Delta R}{L} I_\beta(t_3) - \frac{1}{L}\int_0^{t_3} u_\beta(\tau)d\tau - \frac{\psi}{L}\sin(\theta_0)\right)}{-\left(i_\alpha(t_3) + \frac{\bar{R}+\Delta R}{L} I_\alpha(t_3) - \frac{1}{L}\int_0^{t_3} u_\alpha(\tau)d\tau - \frac{\psi}{L}\cos(\theta_0)\right)}.$$

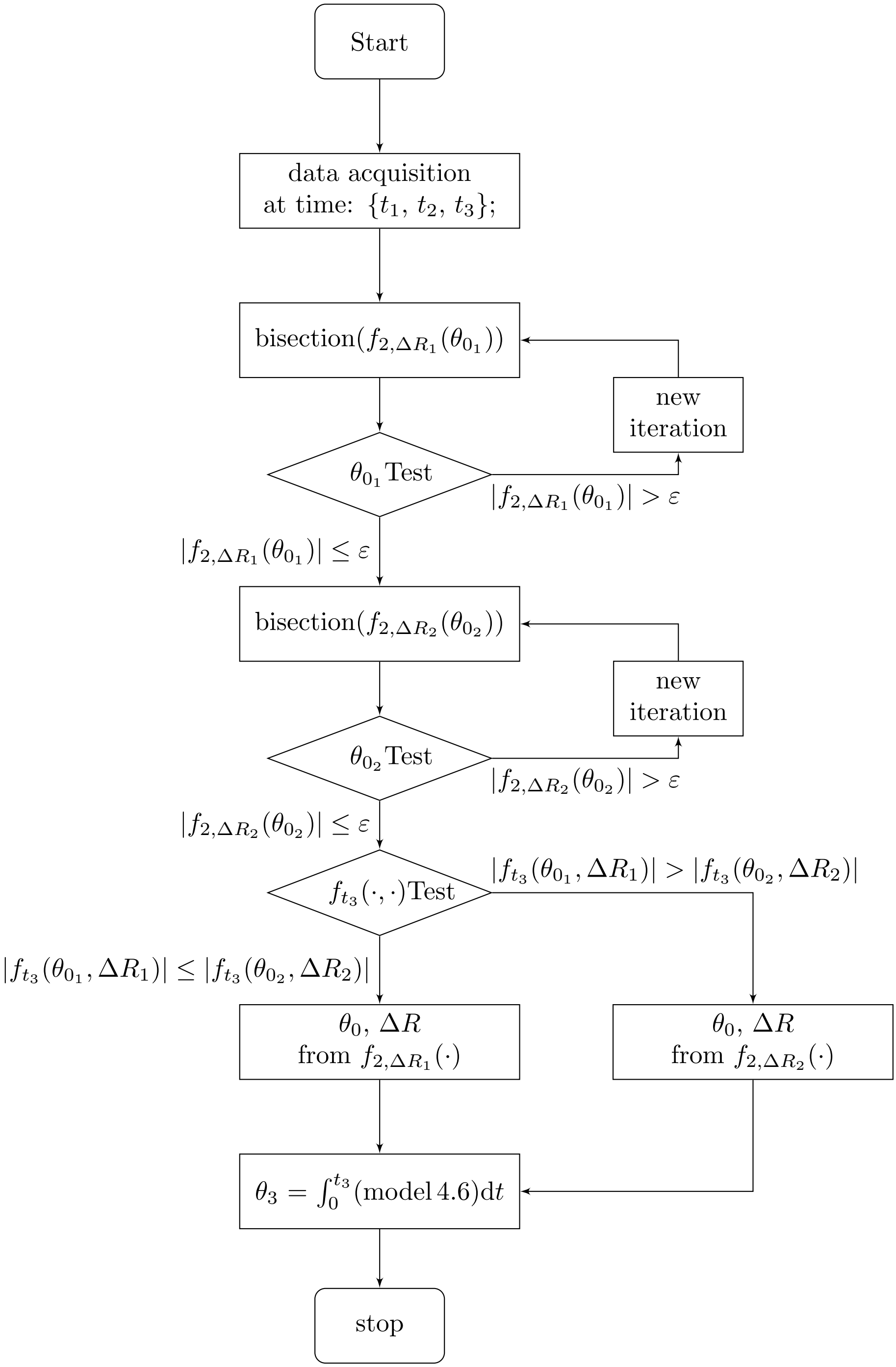
Start
data acquisition at time: $\{t_1, t_2, t_3\}$;
bisection($f_{2,\Delta R_1}(\theta_{0_1})$)
new iteration
θ_{0_1} Test
$|f_{2,\Delta R_1}(\theta_{0_1})| > \varepsilon$
$|f_{2,\Delta R_1}(\theta_{0_1})| \leq \varepsilon$
bisection($f_{2,\Delta R_2}(\theta_{0_2})$)
new iteration
θ_{0_2} Test
$|f_{2,\Delta R_2}(\theta_{0_2})| > \varepsilon$
$|f_{2,\Delta R_2}(\theta_{0_2})| \leq \varepsilon$
$|f_{t_3}(\theta_{0_1}, \Delta R_1)| > |f_{t_3}(\theta_{0_2}, \Delta R_2)|$
$f_{t_3}(\cdot,\cdot)$Test
$|f_{t_3}(\theta_{0_1}, \Delta R_1)| \leq |f_{t_3}(\theta_{0_2}, \Delta R_2)|$
θ_0, ΔR from $f_{2,\Delta R_1}(\cdot)$
θ_0, ΔR from $f_{2,\Delta R_2}(\cdot)$
$\theta_3 = \int_0^{t_3}(\text{model } 4.6)\mathrm{d}t$
stop

Figure 5.1.: Flow chart for numerical solution.

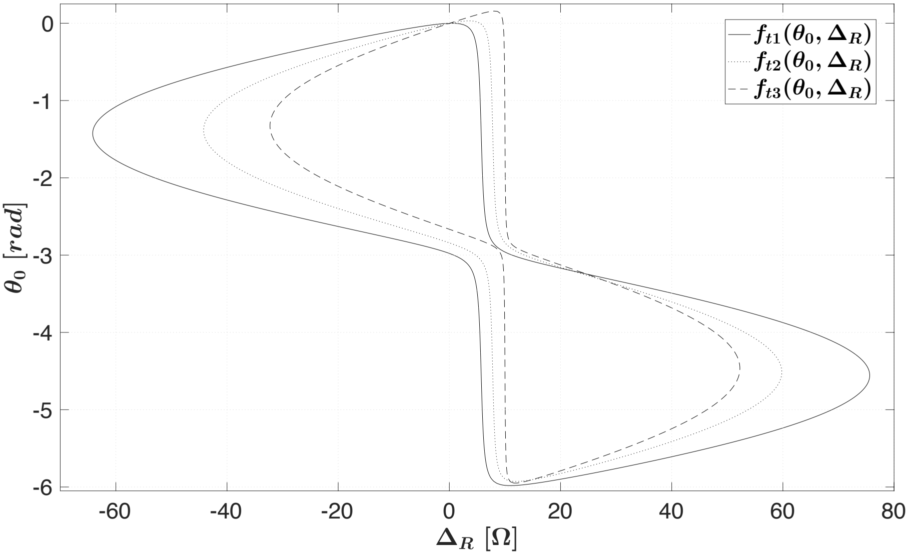

Figure 5.2.: Graphical representation of the system (5.16), case ($\theta_e = 0$, $\Delta R = 0$)

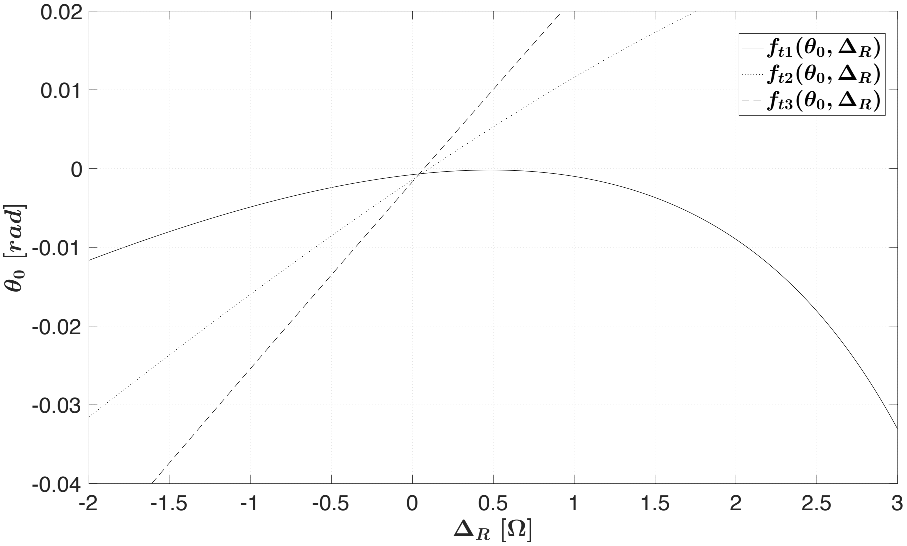

Figure 5.3.: The true intersection point of the Fig. 5.2

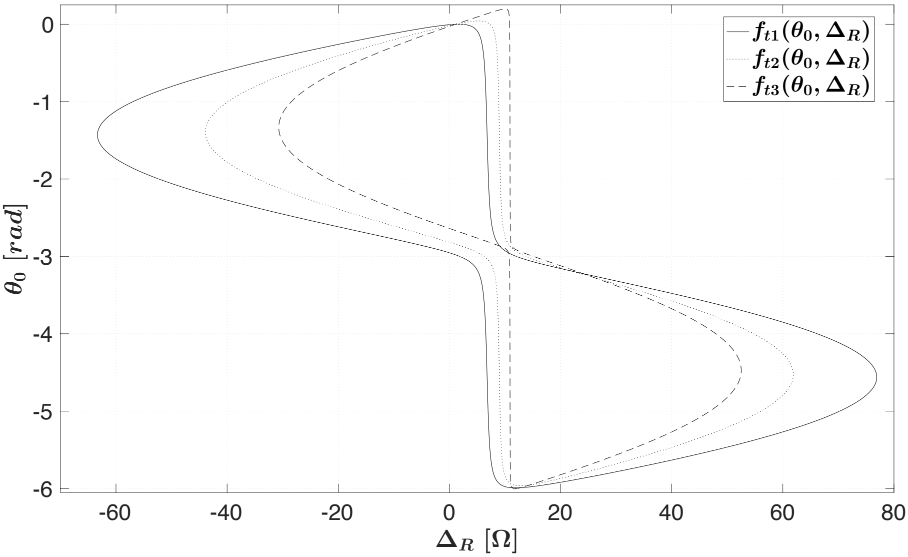

Figure 5.4.: Graphical representation of the system (5.16), case ($\theta_e = 0$, $\Delta R = +10\%$ of $\bar{R}$)

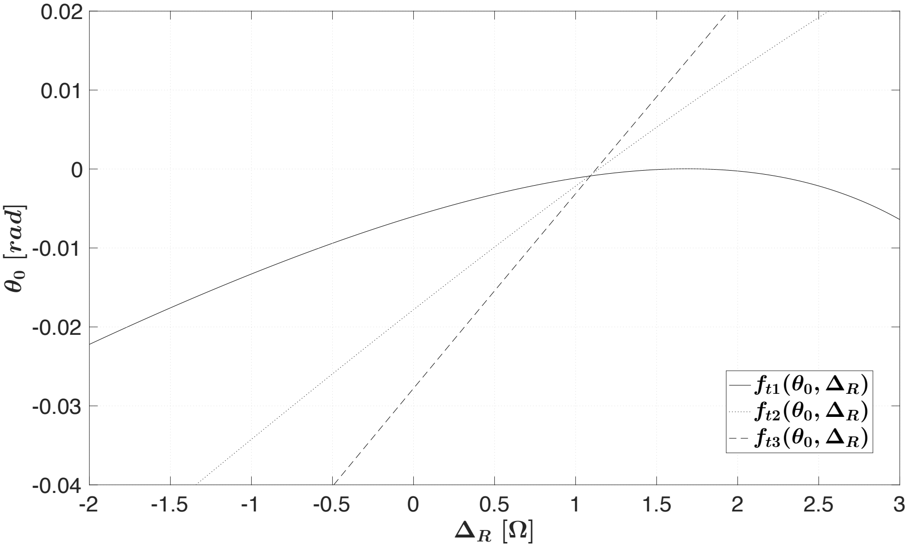

Figure 5.5.: The true intersection point of the Fig. 5.4

5.2. Sliding Mode Control design

5.2.1. Derivation of rotor angular position from currents

In standard drives, rotor position is given by encoder measurements, and rotor speed is usually estimated as the incremental ratio of encoder positions over one sampling period. It will be shown that the angular position of the rotor can be derived from measurements of currents $i_\alpha(t)$ and $i_\beta(t)$.

Remark 5.2.1. *Results reported in the section 5.1 show that ΔR and θ_0 can be exactly determined. Accordingly, the quantity $R = \bar{R} + \Delta R$ will be considered exactly known.*

Consider the following pseudo-observer

$$\begin{cases} \dfrac{d\hat{i}_\alpha(t)}{dt} = -\dfrac{R}{L} i_\alpha(t) + \dfrac{1}{L} u_\alpha(t) \\ \dfrac{d\hat{i}_\beta(t)}{dt} = -\dfrac{R}{L} i_\beta(t) + \dfrac{1}{L} u_\beta(t) \end{cases} \tag{5.17}$$

and define the observation errors:

$$\epsilon_\alpha(t) = i_\alpha(t) - \hat{i}_\alpha(t) \tag{5.18}$$

$$\epsilon_\beta(t) = i_\beta(t) - \hat{i}_\beta(t). \tag{5.19}$$

Lemma 5.2.1. *Referring to plant (4.6), the angular position $\theta_e(t)$ of the rotor can be exactly derived from currents according to*

$$\theta_e(t) = \arctan \frac{-\epsilon_\beta(t) + \dfrac{\psi}{L}\sin(\theta_0)}{-\epsilon_\alpha(t) + \dfrac{\psi}{L}\cos(\theta_0)}. \tag{5.20}$$

Proof. The dynamics of the observation errors are:

$$\dot{\epsilon}_\alpha(t) = \frac{\psi}{L}\omega_e(t)\sin(\theta_e(t)) \tag{5.21}$$

$$\dot{\epsilon}_\beta(t) = -\frac{\psi}{L}\omega_e(t)\cos(\theta_e(t)), \tag{5.22}$$

integrating one gets:

$$\epsilon_\alpha(t) = \epsilon_\alpha(0) - \frac{\psi}{L}\big(\cos(\theta_e(t)) - \cos(\theta_0)\big) \tag{5.23}$$

$$\epsilon_\beta(t) = \epsilon_\beta(0) - \frac{\psi}{L}\big(\sin(\theta_e(t)) - \sin(\theta_0)\big). \tag{5.24}$$

Since the initial condition of the observer (5.17) can be set equal to the initial value of the (measured) currents, it follows that the angular position $\theta_e(t)$ can be computed as in (5.20) [42]. □

Due to Lemma 5.2.1 and to the prior identification of the initial angular position using the algorithm of Section 5.1.2, the angular position $\theta_e(t)$ is a known quantity and can be used for the synthesis of the speed tracking controller.

5.2.2. The sensorless speed-tracking controller

The tracking problem is here considered, *i.e.* the variable $\omega_e(t)$ is required to track a known reference $\omega^*(t)$. The proposed scheme is characterised by two hierarchical levels. The low-level control action corresponds to the design of a current input $I^*(t)$ able to guarantee the robust tracking of the assigned reference in the framework of the FOC scheme, while the high-level controller is responsible to allocate the voltage inputs $u_\alpha(t), u_\beta(t)$ in order to attain the desired current $I^*(t)$. The low-level control design is based on the sliding-surface $s(t) = 0$, with:

$$s(t) = J(\theta_e(t) - \theta^*(t)) \tag{5.25}$$

where $\theta^*(t)$ is the reference rotor position. Integrating equations (4.11)-(4.12) and using (4.10), the time derivative of (5.25) can be computed as follows:

$$\begin{aligned}\dot{s}(t) = J(\omega_e(t) - \omega^*(t)) = -(\bar{B} + \Delta B)(\theta_e(t) - \theta_0) + \hookleftarrow \\ + N_p K' \int_0^t \left[i_\beta(\tau)\cos(\theta_e(\tau)) - i_\alpha(\tau)\sin(\theta_e(\tau)) \right] d\tau + \hookleftarrow \\ - N_p \int_0^t \left[\bar{T}_L(\tau) + \Delta T_L(\tau) \right] d\tau - J\omega^*(t).\end{aligned} \tag{5.26}$$

In (5.26) consider two reference currents:

$$i_\alpha^*(t) = -I^*(t)\sin(\theta_e(t)) \tag{5.27}$$

$$i_\beta^*(t) = I^*(t)\cos(\theta_e(t)), \tag{5.28}$$

whose tracking will be ensured later by the high-level controller, and where $I^*(t)$ is to be determined. When

$$i_\alpha(t) = i_\alpha^*(t) \tag{5.29}$$

$$i_\beta(t) = i_\beta^*(t), \tag{5.30}$$

one has:

$$\begin{aligned}\dot{s}(t) = J(\omega_e(t) - \omega^*(t)) = -(\bar{B} + \Delta B)(\theta_e(t) - \theta_0) + \hookleftarrow \\ +N_p K' v(t) - N_p \int_0^t \left[\bar{T}_L(\tau) + \Delta T_L(\tau)\right] d\tau - J\omega^*(t)\end{aligned} \tag{5.31}$$

being

$$v(t) = \int_0^t I^*(\tau) d\tau. \tag{5.32}$$

Keeping in mind the ideal sliding-mode $s(t) = 0$, the following result can be proved, where the practical condition $|s(t)| \leq \epsilon$ is required for implementation purposes.

Lemma 5.2.2. *Consider a reference speed with* $\omega^*(0) = 0$. *Then, for any* $\epsilon > 0$, *replacing in (5.27) the following control input* $I_\epsilon^*(t)$ *ensures the uniform asymptotic boundedness condition* $|s(t)| \leq \epsilon$ *for the sliding surface (5.25):*

$$\begin{aligned}K I_\epsilon^*(t) = J\dot{\omega}^*(t) + N_p \bar{T}_L(t) - \zeta J \left[(\bar{B} + \rho_B) N_p \omega_e^M + \hookleftarrow\right. \\ \left. +\rho_{T_L}\right] \mathrm{sgn}_\epsilon(s(t)) - \zeta J[(\bar{B} + \rho_B)\omega_e^M + \hookleftarrow \\ + N_p \rho_{T_L}] t \chi_\epsilon(s(t))(D^- \theta_e(t) - \omega^*(t))\end{aligned} \tag{5.33}$$

with $K = N_p K'$, $\zeta > 1$ *and where the function* $\chi_\epsilon(\cdot)$ *and the left derivative* $D^- \theta_e(t)$ *have been defined in (2.8) and (2.9), respectively.*

Proof. Following a classical approach [47], a sliding motion on (5.25) is enforced by $v(t) = v_{eq}(t) + v_n(t)$, where $v_{eq}(t)$ is the control input guaranteeing that $\dot{s}(t) = 0$ in the nominal case corresponding to $\Delta T_L \equiv 0$ and $\Delta B = 0$, *i.e.*

$$K v_{eq}(t) = J\omega^*(t) + N_p \int_0^t \bar{T}_L(\tau) d\tau + \bar{B}(\theta_e(t) - \theta_0), \tag{5.34}$$

while the discontinuous input signal $v_n(t)$ is designed to ensure:

$$s(t)\dot{s}(t) < 0 \qquad \forall t. \tag{5.35}$$

In particular, the introduction of (5.34) into (5.31) provides

$$\begin{aligned}s(t)\dot{s}(t) = s(t)\Big(- \Delta B(\theta_e(t) - \theta_0) + K v_n(t) + \hookleftarrow \\ -N_p \int_0^t \left[\Delta T_L(\tau)\right] d\tau\Big) < 0.\end{aligned} \tag{5.36}$$

Setting $s(t) > 0$ and taking the worst case, noticing that

$$|\theta_e(t) - \theta_0| < \omega_e^M t,$$

one gets

$$K' v_n(t) = -\zeta \left[\rho_B \omega_e^M t + N_p \rho_{T_L} t\right] \operatorname{sgn}(s(t)) \tag{5.37}$$

with $\zeta > 1$. The same result is obtained for $s(t) < 0$. On the other hand, since the control $v(t)$ is assigned by (5.32), it is not allowed to be discontinuous and a sliding-mode cannot be properly enforced. In order to satisfy the requested regularity conditions, the function $\operatorname{sgn}(s(t))$ can be replaced by its approximation $\operatorname{sgn}_\epsilon(s(t))$ given by (2.7). Let us denote by $v_{n,\epsilon}(t)$ such regularized controller. By construction, since $|\theta_e(t) - \theta_0| \leq \omega_e^M t$, the control law $v(t) = v_{eq}(t) + v_{n,\epsilon}(t)$ guarantees the uniform boundedness condition $|s(t)| \leq \epsilon, \quad \forall t \geq T_\epsilon > 0$, and it is straightforward that:

$$\operatorname{sgn}_\epsilon(s(t)) = J \int_0^t \chi_\epsilon(s(\tau))(D^- \theta_e(\tau) - \omega^*(\tau)) d\tau. \tag{5.38}$$

This shows that $K' I_\epsilon^*(t) = \dot{v}_{n,\epsilon}(t)$, therefore the expression (5.33) can be immediately derived. □

For any $\epsilon > 0$ the derivative $\frac{d}{dz}\chi_\epsilon(z)$ exists almost everywhere and it satisfies

$$\left| \frac{d}{dz}\chi_\epsilon(z) \right| \leq \frac{2}{\epsilon^2} \qquad \forall z \in \mathbb{R}. \tag{5.39}$$

As a consequence the left-derivative $D^- I_\epsilon^*(t)$ is well defined and it verifies

$$\begin{aligned} K' D^- I_\epsilon^*(t) = J \ddot{\omega}^*(t) + N_p \dot{T}_L(t) - \zeta J N_p \rho_{T_L} \frac{d}{dz}\chi_\epsilon(s(t)) \Big(D^- \theta_e(t) + \hookleftarrow \\ -\omega^*(t)\Big)^2 - \zeta J N_p \rho_{T_L} \chi_\epsilon(s(t))(D^{2,-}\theta_e(t) - \dot{\omega}^*(t)), \end{aligned} \tag{5.40}$$

where $D^{2,-}\theta_e(t)$ is given by formula (2.10). The following result summarises the control strategy for the robust tracking of an assigned reference velocity, in the presence of bounded perturbations affecting the motor parameters and the load.

Theorem 5.2.1. *With reference to the plant* (4.6) *under Assumption (A.1), the following control inputs $u_\alpha(t)$, $u_\beta(t)$ ensure the (practical) robust tracking of an assigned reference velocity $\omega^*(t)$ using only measurements of the electrical variables of the motor (i.e. sensorless control):*

$$\begin{aligned} \frac{1}{L} u_\alpha(t) = & \frac{R}{L} i_\alpha(t) - D^- I_\epsilon^*(t) \sin(\theta_e(t)) + \hookleftarrow \\ & - \omega_e^M \zeta \left[\frac{\psi}{L} |\sin(\theta_e(t))| + |I_\epsilon^*(t) \cos(\theta_e(t))| \right] \cdot \hookleftarrow \\ & \operatorname{sgn}(i_\alpha(t) + I_\epsilon^*(t) \sin(\theta_e(t))) \end{aligned} \tag{5.41}$$

$$\begin{aligned}\frac{1}{L}u_\beta(t) = {} & \frac{R}{L}i_\beta(t) + D^- I_\epsilon^*(t)\cos(\theta_e(t)) + \hookleftarrow \\ & -\omega_e^M\zeta\left[\frac{\psi}{L}|\cos(\theta_e(t))| + |I_\epsilon^*(t)\sin(\theta_e(t))|\right]\cdot \hookleftarrow \\ & \operatorname{sgn}(i_\beta(t) - I_\epsilon^*(t)\cos(\theta_e(t))), \quad \zeta > 1;\end{aligned} \tag{5.42}$$

where the current input $I_\epsilon^*(t)$ is assigned by (5.33).

Proof. The overall closed-loop stability can be proved using standard Lyapunov techniques, imposing $i_\alpha(t) = i_\alpha^*(t)$, $i_\beta(t) = i_\beta^*(t)$ by the following Lyapunov function:

$$Y(t) = \frac{1}{2}\left[i_\alpha(t) - i_\alpha^*(t)\right]^2 + \frac{1}{2}\left[i_\beta(t) - i_\beta^*(t)\right]^2 \tag{5.43}$$

and observing that, if $u_\alpha(t)$ and $u_\beta(t)$ are chosen according to (5.41)-(5.42), then the inequality $\dot{Y}(t) < 0$ holds. In fact, define:

$$\begin{aligned}\eta_\alpha(t) &= i_\alpha(t) - i_\alpha^*(t) \\ \eta_\beta(t) &= i_\beta(t) - i_\beta^*(t).\end{aligned}$$

Since $\dot{Y}(t) = \eta_\alpha(t)\dot{\eta}_\alpha(t) + \eta_\beta(t)\dot{\eta}_\beta(t)$, consider the imposition of $\eta_\alpha(t)\dot{\eta}_\alpha(t) < 0$. One gets, in the case $\eta_\alpha(t) = i_\alpha(t) + I_\epsilon^*(t)\sin(\theta_e(t)) > 0$

$$-\frac{R}{L}i_\alpha(t) + \omega_e(t)\frac{\psi}{L}\sin(\theta_e(t)) + \frac{1}{L}u_\alpha(t) + D^-\left[I_\epsilon^*(t)\sin(\theta_e(t))\right] < 0. \tag{5.44}$$

It can be easily verified that the control law (5.41) satisfies the previous inequality. Following an analogous approach for the case $\eta_\alpha(t) < 0$, the expression (5.41) immediately follows. The expression of (5.42) can be obtained analogously imposing the condition $\eta_\beta(t)\dot{\eta}_\beta(t) < 0$. □

Chapter 6.

Setup and Results

6.1. Experimental setup

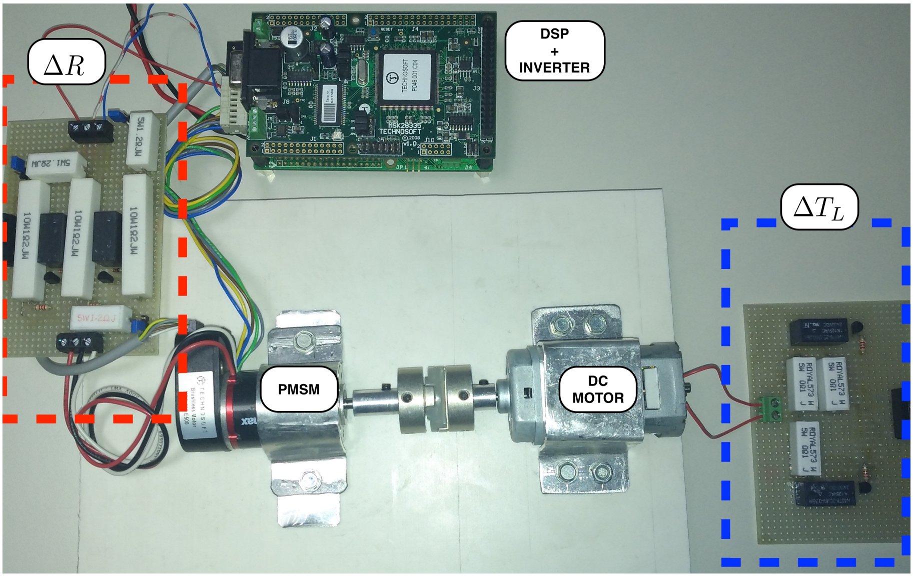

ΔR
DSP + INVERTER
ΔT_L
PMSM
DC MOTOR

Figure 6.1.: Hardware setup.

Table 6.1.: Technosoft© MBE.300.E500 PMSM parameters.

Coil dependent parameters		
line-to-line resistance	Ω	8.61
line-to-line inductance	mH	0.713
Back-EMF constant	V/kRPM	3.86
Torque constant	mNm/A	36.8
Pole pairs	–	1
Dynamic parameters		
Rated voltage	V	36
Max. voltage	V	58
No-load current	mA	73.2
No-load speed	RPM	9170
Max. cont. current (at 5 kRPM)	mA	913
Max. cont. torque (at 5 kRPM)	mNm	30
Max. permissible speed	RPM	15000
Peak torque (stall)	mNm	154
Mechanical parameters		
Rotor inertia	$k$gm^2	$11\cdot10^{-7}$
Mechanical time constant	ms	7

The experimental setup, as show Fig. 6.1, includes a DSP-based controller board, a power module, a PMSM equipped with a 500-line encoder and a software platform to develop motion control applications. Experiments have been carried out using the Technosoft MBE.300.E500 PMSM. The electric and mechanical parameters have been listed in Tab.6.1 [48]. The Technosoft PM50 power module includes a 3-phase inverter, the protection circuits and the measurement circuits for the DC-bus voltage and the motor currents. The 3-phase inverter uses MOSFET transistors with switching frequency up to 50 [kHz]. The control unit is the Technosoft MSK28335 board based on the high performance Texas Instruments TMS320F28335 DSP motion controller. The three-phase voltage commands are generated using the outputs of the PWM unit, applied to the 6 transistors of the power inverter (see Fig. 6.2). The DSP has a 150 MIPS, 32 bit floating point DSP core and operates at a 150 [MHz] frequency. The MSK28335 board is equipped also with 128-kWords 0-wait state external RAM, 2 channels of 12-bit accuracy D/A outputs, 16 channels of 12-bit accuracy A/D inputs, RS-232, CAN-bus and JTAG interfaces. The sampling frequency is selected as 1 [kHz] for the velocity control loop and 10 [kHz] for the current control loops. The MCK28335-Pro kit includes the DMCD28x-Pro, the Technosoft software platform, which allows the development of motor control applications. The code is developed in C language using a modular approach providing flexibility for further system integration. The control architecture is shown in Fig. 6.2: two mechanically coupled motors, *i.e.* a PMSM

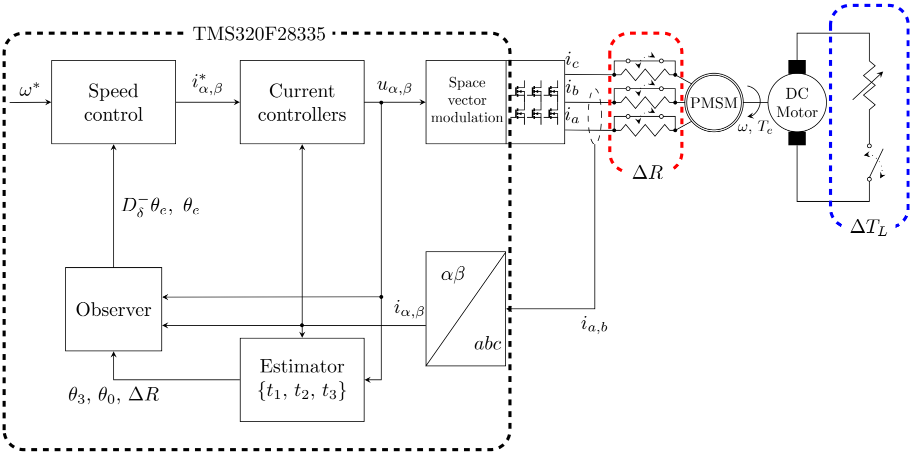
TMS320F28335
ω^*
Speed control
$i^*_{\alpha,\beta}$
Current controllers
$u_{\alpha,\beta}$
Space vector modulation
i_c
i_b
i_a
PMSM
DC Motor
ω, T_e
ΔR
ΔT_L
$D^-_\delta\theta_e$, θ_e
Observer
$\alpha\beta$
abc
$i_{\alpha,\beta}$
$i_{a,b}$
Estimator $\{t_1, t_2, t_3\}$
θ_3, θ_0, ΔR

Figure 6.2.: Block scheme of the sensorless control.

and a DC Motor, are present: the master (PMSM) is controlled according to the proposed control law, and the slave (DC motor) is used in brake mode, to generate the torque disturbance. Moreover, the resistance variation (ΔR) has been obtained connecting an external resistor circuit in-line with the motor phases. The torque disturbance and the resistance variation have been used to evaluate the performance of the control scheme.

6.2. Results

In order to perform experiments with the sensorless control technique using the DSP board, a preliminary step is required. In particular, the PMSM has to be open-loop started and the signals used to drive the motor are shown in Fig. 6.3. In this time interval, the algorithm solves the equations (5.16), and the numerical solutions are reported in Tab. 6.2. Once these solutions have been computed, the proposed robust sensorless speed controller can be enabled and tested. Two speed profiles, *i.e.* a trapezoidal and a sine waveforms, have been considered as shown in Figs. 6.4(a) and 6.6(a). In both tests, the torque disturbance and the resistance variation have been started in five different time intervals, *i.e.* [1.05 to 2.05] [s], [3.55 to 4.55] [s], [6.05 to 7.05] [s] and [8.55 to 9.55] [s] for a torque disturbance of 33 [mNm], and [10.3 to 15.3] [s] for a resistance variation $\Delta R = 2.4$ [Ω].

The experimental results are reported in Figs. 6.4-6.7: figure 6.4(a) shows the speed tracking performances with a trapezoidal reference, while Figs. 6.4(b) and 6.4(c) zoom into the previous picture, showing the good behavior of the sensorless control under the torque disturbances. The control inputs u_α and

u_β are reported in Fig. 6.5(a). The intervals 0.8 [s] to 1.3 [s] and 3.3 [s] to 3.8 [s], (Figs. 6.5(b) and 6.5(c), respectively), show u_α and u_β under the torque disturbances, while the interval 10 [s] to 11 [s], of Fig. 6.5(d), shows u_α and u_β under the resistance variation. The same tests have been repeated using a sinusoidal reference, obtaining analogous results, reported in Figs. 6.6(a), 6.6(b), 6.6(c), 6.7(a), 6.7(b), 6.7(c), 6.7(d). The numerical solutions after the resistance variation are tabled in Tab.6.2.

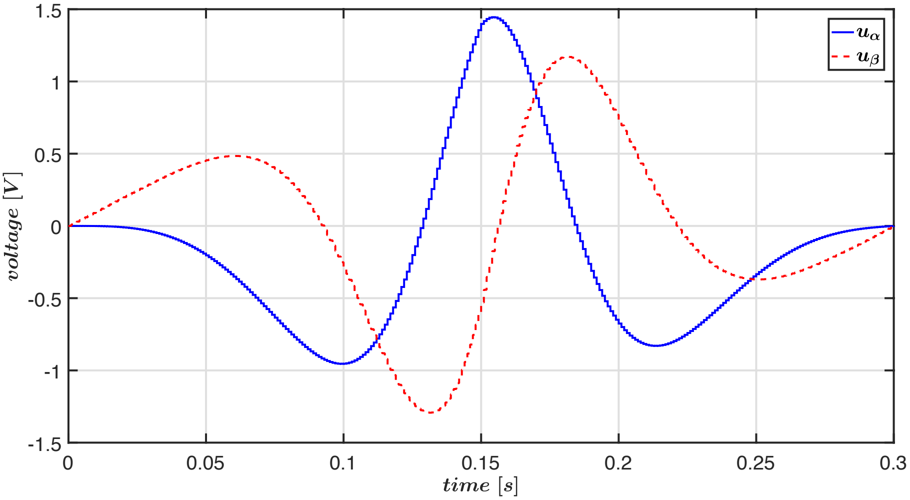

Figure 6.3.: Signals used to drive open loop the motor, u_α (continuous blue-line) and u_β (dashed red-line).

Table 6.2.: Numerical solutions.

TEST	ΔR [Ω]	θ_0 [rad]	θ_3 [rad]	ΔR@10.3[s] [Ω]
Trapezoidal	0.0230	0.0125	3.0191	2.4103
Sinusoidal	0.0271	0.0141	3.0137	2.3877

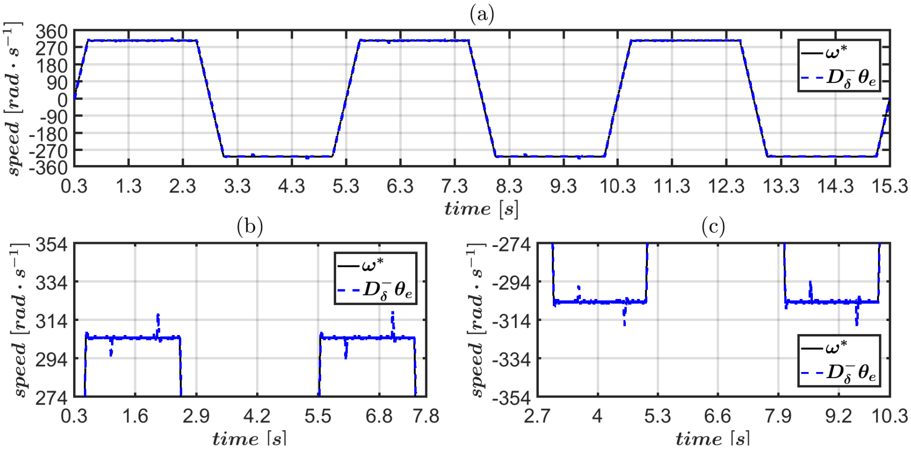

Figure 6.4.: (a): speed tracking with a trapezoidal reference, ω^* (continuous black-line) and $D_\delta^- \theta_e$ (dashed blue-line); (b) and (c): zoom of the behaviours of the sensorless control under torque disturbances.

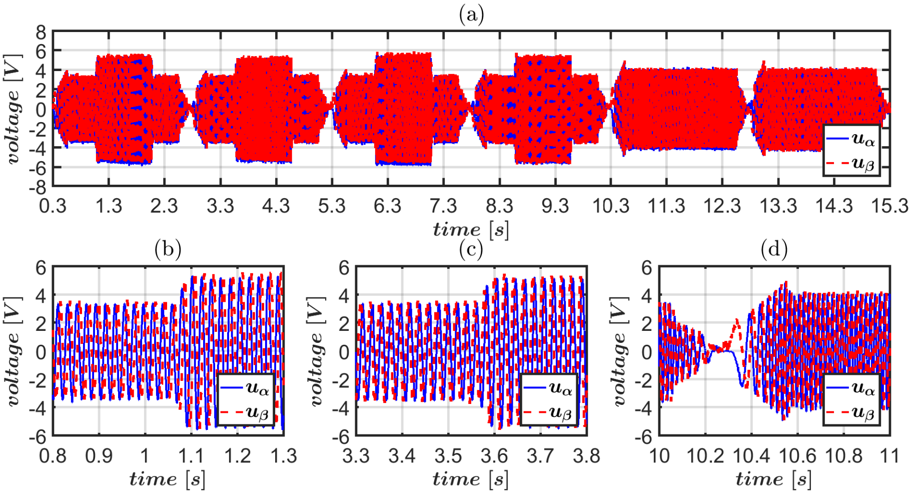

Figure 6.5.: (a): control inputs u_α (continuous blue-line) and u_β (dashed red-line) for the trapezoidal reference; (b) and (c): control inputs due to the torque disturbances; (d): control inputs due to the resistance variation.

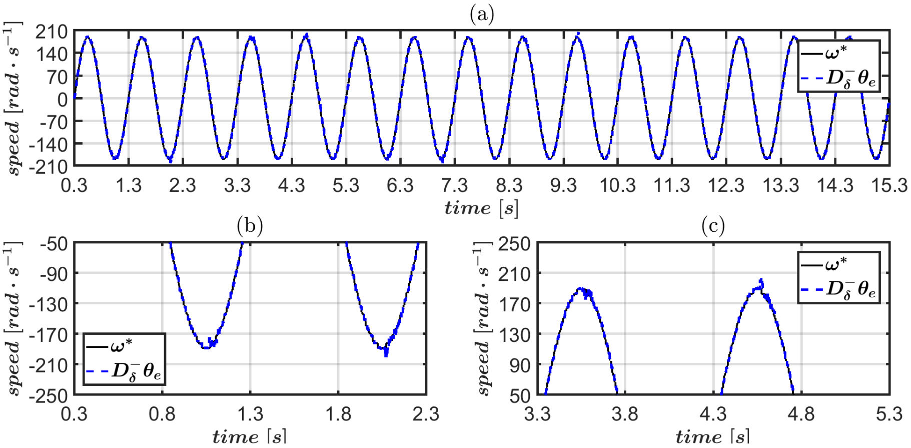

Figure 6.6.: (a): speed tracking with a sinusoidal reference, ω^* (continuous black-line) and $D_\delta^- \theta_e$ (dashed blue-line); (b) and (c): zoom of the behaviours of the sensorless control under torque disturbances.

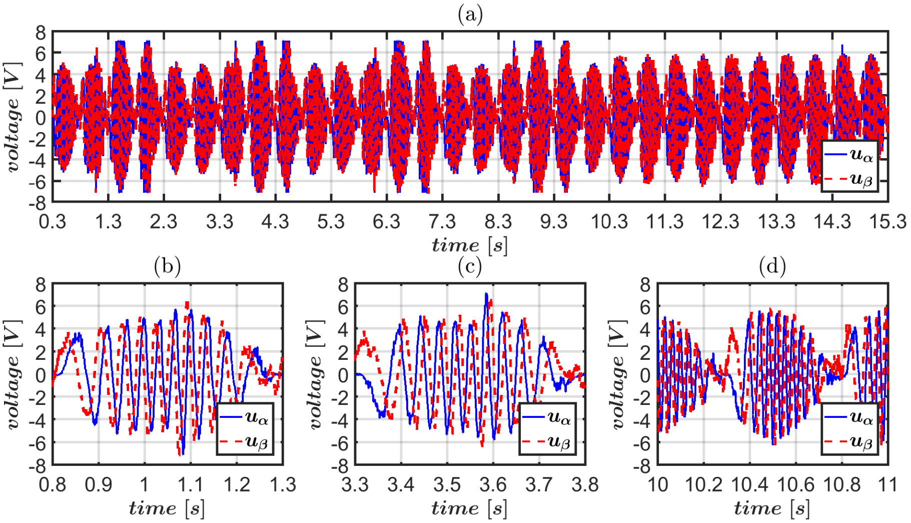

Figure 6.7.: (a) control inputs u_α (continuous blue-line) and u_β (dashed red-line) for the sinusoidal reference; (b) and (c): control inputs due to the torque disturbances; (d): control inputs due to the resistance variation.

6.2.1. Flops overview

The digital signal processor (DSP) used in the experimental results is the TMS320F28335 by Texas Instruments with a core at 150 [MHz]. Its computational effort is 300 [MFLOPS], which means that the DSP can compute up to $300 \cdot 10^6$ operations for each cycle, such as addition, multiplication, data movement and value testing. The computational burden of the proposed algorithm has been quantified in flops, following the order of the executed operations, as explained below. At the beginning of the algorithm, the electrical signals ($i_{\alpha,\,\beta}$, $u_{\alpha,\,\beta}$) are numerically integrated. This implies a computational burden given by the following equation:

$$(t_3[\mathrm{s}] \cdot 10 \times 10^3[\mathrm{Hz}] + 1) \cdot 5 \cdot 4 \text{ [FLOPS]} \tag{6.1}$$

where 4 is the number of signals to be considered, *i.e.* ($i_{\alpha,\,\beta}$, $u_{\alpha,\,\beta}$), 5 is the number of basic operations required by the numeric integration and $(t_3[\mathrm{s}] \cdot 10 \times 10^3[\mathrm{Hz}] + 1)$ is the times that the basic operations have to be repeated during the numeric integration. In the experimental results $t_3 = 300$ [ms] that implies 60.02 [kFLOPS] of computational effort. For the construction of the matrices $W(t)$, $E(t)$ in (5.7), and to create the functions $f_{2,\Delta R_1}(\theta_{0_1})$, $f_{2,\Delta R_2}(\theta_{0_2})$ in Fig. 5.1, 42 [FLOPS] and 28 [FLOPS] are used, respectively. The functions $f_{2,\Delta R_1}(\theta_{0_1})$, $f_{2,\Delta R_2}(\theta_{0_2})$ have been evaluated by the bisection method, providing for each function the following number of iterations:

$$N_{max} = \left\lceil \frac{|\log(b-a) - \log(Tol.)|}{\log 2} \right\rceil , \tag{6.2}$$

where N_{max} denotes the maximum number of iterations in the bisection method, $(b-a) = \pi$ is the distance between the extremes of the interval $(b,\, a)$ and $Tol.$ is the given tolerance equal to 10^{-4}. It follows that, the number of flops is $N_{max} \cdot 14 \cdot 2$ [FLOPS], being the function evaluated two times at each iteration. If the algorithm fails to find a solution in the range $[0,\, \pi]$, the search of the roots is carried out in the complementary one $[\pi,\, 2\pi]$. Consequently the maximum number of flops is $(N_{max} + 1) \cdot 14 \cdot 2$ [FLOPS], namely 448 [FLOPS] for each function. In both cases N_{max} is equal to 15. The best solution is chosen using the third equation of the system (5.16), whose operation requires 28 [FLOPS]. Finally, the computation of θ_3 requires 132 [FLOPS], *i.e.* 118 [FLOPS] for the computation of $\mathrm{atan2}(\mathrm{y},\ \mathrm{x})$ and 7 [FLOPS] for each argument of $\mathrm{atan2}(\cdot, \cdot)$. In conclusion, the computational burden of the proposed algorithm is 61.146 [kFLOPS] which is fairly low with respect to the computational effort of 300 [MFLOPS] supported by the DSP.

As far as the existence of feasible solutions is concerned, Theorem 5.1.1 proves that, under weak conditions, four solutions exist for the system (5.16).

Indeed, the rank condition (5.9) is generically fulfilled: in particular, under a classical persistency of excitation condition, almost every triple $\{t_1, t_2, t_3\}$ with $t_1 < t_2 < t_3$ satisfies the desired rank requirement. It is worth to note that, in many cases, the system admits the true solution $(\cos\theta_0, \sin\theta_0, \Delta R)$ only: this is a consequence of the strong constraint given by the fourth equation. Moreover, since by construction the pair of actual values $(\theta_0, \Delta R)$ is a solution to the system for any value of t, a confirmation and/or a refinement to avoid biased estimation due to noisy measurement can be attained by considering additional time steps. On the other hand, if it is not possible to isolate the true solution by means of algebraic methods, one can introduce the decision algorithm based on multiple models, each one being associated to a feasible solution as described in the section 5.1.1.

Part II.

Black-Box Approach

Chapter 7.

Introduction

Piezoelectric actuators (PAs) are featured by high-frequency, fast dynamics and string stiffness united to the ultra-fine resolution [49] that allows to use this technology in several fields requiring high-accuracy movements [50] (biological and atomic microscopy, micromanipulation and nanopositioning applications [51–54]). PA systems also present different behaviour issues due to system mechanics problems, such as hysteresis [55,56], vibration phenomenons [57] and output placement drift [58]. Despite these problems, PAs' nominal positioning accuracy and displacement features can be improved by several control techniques [52], overcoming system mechanical disadvantages and guaranteeing prescribed performances. Considering the high fidelity dynamical models of PAs and the related undesired phenomena [59–61] several advanced control techniques have been proposed by the research community, such as adaptive control [62–64], sliding mode control [65–68] or H_∞ control [69, 70]. Anyway standard commercial PAs systems and instruments are still provided with conventional Proportional-Integral (PI) controllers, allowing to guarantee prescribed stability margins in presence of noise and disturbances [71]. These PI controllers are often provided in an analog implementation in order to not introduce delays in system response, but usually they cannot be easily tuned on the considered system, and obtained control performances do not reflect nominal features [72].

In this activity has been proposed to improve control performances provided by standard PI controllers by the introduction of an external control loop based on the Linear Quadratic Gaussian (LQG) control policy. LQG is a well known technique in the field of PAs plants [73–75] due to the linear input-output behaviour of this kind of systems. Based on the idea of Reference Governor (RG) [76], this thesis presents the design of a LQG controller that regulates a PI pre-compensated PA system manipulating the reference signal [76,77]. The research related to RG includes several engineering fields, such as robotics [78], automotive [79] and power electronics [80] but current studies on PAs devices are focused on the substitution of the standard controller [81]. Instead, in PAs commercial applications it is preferred to maintain provided PI controllers, avoiding to replace it with alternative advanced regulators, because of: *i*) usually PAs systems' stakeholders do not consider positioning accuracy improvable, *ii*) theoretically PI could be tuned to provide an arbitrary small response time, even if the controller implementation results impossible for very high gains [82].

7.1. Problem statement

The main features of the proposed strategy can be summarised as follows:

(P.1) It identifies a numerical model containing any *couplings between the axes.*

(P.2) It increases system *performance* of the commercial actuator.

The proposed approach introduces an external control loop allowing to improve PI control performances overcoming previous limits, maintaining the native low level controller and introducing a small additive computational effort.

The solution has been tested on a commercial PAs system. The experimental setup considers a 3-DOF micro-nano resolution piezoelectric actuators system driven by an external control amplifier that provides a set of analog PI controllers. The system is modelled in the form of a Linear Time Invariant (LTI) Multi-Input Multi-Output (MIMO) plant obtained by an identification procedure applied to the closed loop system. System identification is a standard solution for modelling piezoelectric systems due to the linear input-output behaviour of real plant [83–85]. The identified system model is used to design the external LQG control loop and to verify it in simulation tests before to switch to the experimental validation.

Chapter 8.

The Mathematical Model and Control Design

In this chapter, the mathematical model of the piezoelectric actuator for a single axis is introduced. The overall dynamics, relating to all three axes, is obtained by considering three parallel models. It is assumed that the dynamics for each axis is decoupled from the dynamics of the other axes. The dynamics of the piezoelectric motor can be represented by the following system of second-order differential equations in the presence of hysteresis and external forces:

$$m\ddot{x}(t) + c\dot{x} + kx = T\left(u(t) - h(t)\right) - F_e(t) + p(t), \tag{8.1}$$

$$\begin{gathered} x(t) \in \mathscr{X} \simeq \mathbb{R}, \quad u(t) \in \mathscr{U} \simeq \mathbb{R}, \quad m, c, k \in \mathscr{P} \simeq \mathbb{R}^+, \\ h(t), F_e(t), p(t) \in \mathscr{D} \simeq \mathbb{R}, \end{gathered}$$

where m represents the mass of the actuator, $x(t)$ is the displacement of the stage, c and k are the damping and stiffness coefficients, T denotes the electromechanical ratio, $u(t)$ is the control input, $h(t)$ is the non-linear model of the hysteresis, $F_e(t)$ summarises the external forces, while $p(t)$ models the overall perturbations acting on the system due to the uncertainty of the parameters, to unmodeled dynamics and other unknown terms.

8.1. The hysteresis

In piezoelectric actuators and many other physical systems, the hysteresis behaviour is the consequence of the presence of elements that accumulate energy and others that dissipate it. On a mechanical level, this behaviour can be obtained by combining two parts in a single system, like an ideal spring with a Coulomb friction element, which represent the quantity of energy-storage and the dissipative part, respectively. This analogy underpins the behaviour of the hysteresis exhibited by the piezoelectric actuators. In (8.1), the representation with concentrated parameters Maxwell Resistive Capacitor (MRC) [86] has been considered to model the hysteresis.

8.2. Identification of the pre-compensated system

In spite of the complete mathematical description made in Chapter 8, we found ourselves faced with several problems, *i.e.* axes coupling, unknown process parameters and the unknown model of the commercial controller. These issues have been outflanking by exploiting the black box approach, That is, the whole model, piezoactuator with its controller, has been identified.

For the identification procedure, input references for the PI pre-compensated plant, referred to the X, Y and Z axis drivers, are named r_1, r_2 and r_3, respectively. The measured output displacements are y_1 (X axis), y_2 (Y axis) and y_3 (Z axis). Signals data are acquired with a sampling rate of 20 [kHz]. The identification is realised forcing the closed-loop real plant, driven by the analog PI controller, by several sets of input steps and recording the related outputs. Reference signals have time duration bigger than the settling time of the open-loop system, considered of 120 [ms]. The smaller reference rate causing a detectable output variations is $|\Delta u_i| \geq 0.05$ V and the input signals bounds are $u_i \in [-1, 10]$ [V] with $i \in \{1, 2, 3\}$. During the data acquisition the axis drivers were forced together in order to model any possible coupling effects between the axes. Collected input and output data are used to identify a LTI plant model by a least square identification algorithm. The identified model is tested comparing the computed outputs of the LTI plant model with respect to different sets of acquired data not considered in the identification procedure. Considering the difference between the computed and the acquired outputs, validation tests results are evaluated in terms of the Normalised Root Mean Square Error (NRMSE). The goodness of the identified model is proven by a NRMSE average value of 95%.

In Fig. 8.1 and Fig. 8.2 validation tests results are presented. Output data computed by the identified LTI model are indicated in Fig. 8.1 by y_{m_1}, y_{m_2} and y_{m_3} for X, Y, and Z axis, respectively. Results in figures show how the identified model fits with good precision the measured outputs. In particular Fig. 8.1 shows the fit between the real plant and the identified model forced by steps of fixed amplitude. Figure 8.2 shows the errors (e_x, e_y and e_z) between the outputs of the identified LTI model and the outputs of the real plant. The reduced amplitude of the errors (average value of 0 [μm] and variance of 0.002 [μm], equal to the 1% of the amplitude of the signal variation) proves the goodness of the model. The proposed LQG controllers have been tuned on the identified discrete LTI model:

$$\begin{aligned} \boldsymbol{x}(k+1) &= \boldsymbol{A}\boldsymbol{x}(k) + \boldsymbol{B}\boldsymbol{r}(k) \\ \boldsymbol{y}(k) &= \boldsymbol{C}\boldsymbol{x}(k) \end{aligned} \tag{8.2}$$

where $\boldsymbol{A}$, $\boldsymbol{B}$, $\boldsymbol{C}$ are the identified matrices, $\boldsymbol{r}(k) = \begin{bmatrix} r_1(k) & r_2(k) & r_3(k) \end{bmatrix}^T$ is the reference vector for the PI pre-compensated system of dimension $n_r = 3$, $\boldsymbol{y}(k) = \begin{bmatrix} y_1(k) & y_2(k) & y_3(k) \end{bmatrix}^T$ is the output vector with dimension $n_y = 3$, the number of state variables is $n_x = 6$ and the sample time is $T_s = 50\ \mu s$.

$$\boldsymbol{A} = \left[\begin{matrix} 0.9961 & -1.028\times10^{-5} & 2.097\times10^{-5} \\ -1.005\times10^{-5} & 0.996 & -5.441\times10^{-5} \\ 1.762\times10^{-5} & -5.318\times10^{-5} & 0.996 \\ -0.01154 & -0.6618\times10^{-3} & 1.086\times10^{-3} \\ -0.7019\times10^{-3} & 0.01194 & -0.1237\times10^{-3} \\ 0.7606\times10^{-3} & 1.772\times10^{-3} & 0.01202 \end{matrix}\right.$$

$$\left.\begin{matrix} 0.3409\times10^{-3} & 0.2338\times10^{-3} & -0.2684\times10^{-3} \\ 0.1856\times10^{-3} & -0.3317\times10^{-3} & -0.3943\times10^{-3} \\ -0.279\times10^{-3} & 0.4544\times10^{-3} & -0.3304\times10^{-3} \\ 0.9955 & 2.549\times10^{-5} & -8.17\times10^{-5} \\ 8.395\times10^{-5} & 0.9951 & -0.3366\times10^{-3} \\ -0.2036\times10^{-3} & -0.2215\times10^{-3} & 0.9949 \end{matrix}\right]$$

$$\boldsymbol{B} = \begin{bmatrix} -1.168\times10^{-10} & 1.246\times10^{-9} & 1.361\times10^{-6} \\ -4.463\times10^{-10} & -4.477\times10^{-7} & 1.172\times10^{-9} \\ -7.828\times10^{-7} & 1.33\times10^{-9} & -1.101\times10^{-9} \\ -9.337\times10^{-8} & -1.204\times10^{-6} & 0.1244\times10^{-3} \\ -1.371\times10^{-7} & 0.1426\times10^{-3} & 1.05\times10^{-6} \\ 0.1323\times10^{-3} & 1.454\times10^{-7} & 8.88\times10^{-8} \end{bmatrix}$$

$$\boldsymbol{C} = \begin{bmatrix} 0.0456 & 0.1108 & -135.4613 \\ 0.1199 & -132.1904 & -0.1133 \\ 133.7195 & 0.1185 & 0.0463 \\ 0.2\times10^{-3} & 1.2\times10^{-3} & 0.0575 \\ 0.1\times10^{-3} & -0.1465 & 0.5\times10^{-3} \\ -0.7\times10^{-3} & -0.3\times10^{-3} & 0.4\times10^{-3} \end{bmatrix}^T$$

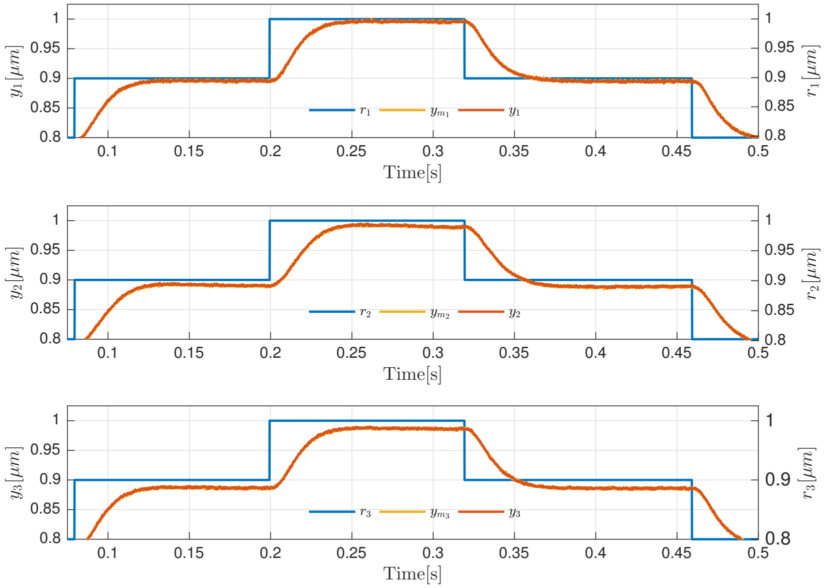

Figure 8.1.: Identification test results, with step input signals.

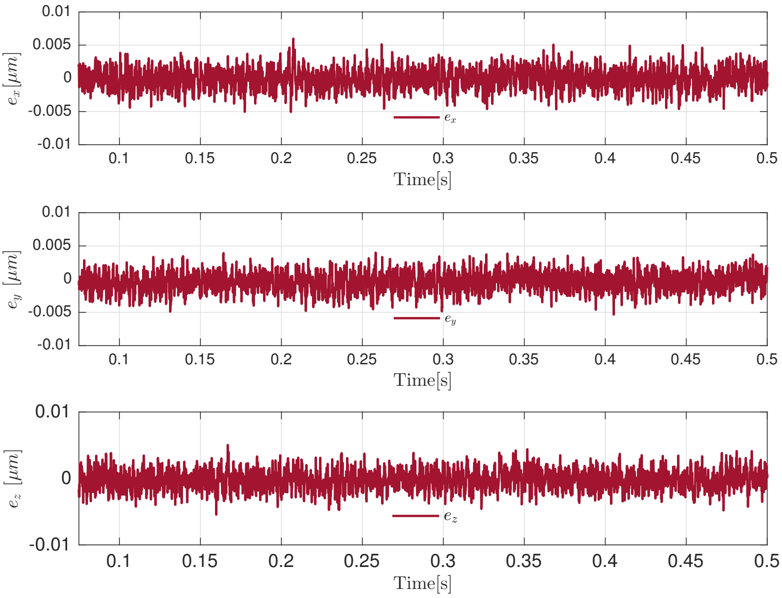

Figure 8.2.: Identification test results, with step input signals.

8.3. LQG design

Considering the identified LTI plant (8.2), the proposed LQG controller minimises iteratively a quadratic cost function defined as

$$\min_{\Delta \boldsymbol{r}} \quad \sum_{i=0}^{N-1} \|\boldsymbol{Q}(\boldsymbol{y}_{k+i|k} - \bar{\boldsymbol{r}}_k)\|_2^2 + \|\boldsymbol{R}\boldsymbol{r}_{k+i|k}\|_2^2 \tag{8.3a}$$

$$\text{s.t.} \quad \boldsymbol{x}_{k|k} = \boldsymbol{x}(k), \tag{8.3b}$$

$$\boldsymbol{x}_{k+i+1|k} = \boldsymbol{A}\boldsymbol{x}_{k+i|k} + \boldsymbol{B}\boldsymbol{r}_{k+i|k}, \tag{8.3c}$$

$$\boldsymbol{y}_{k+i+1|k} = \boldsymbol{C}\boldsymbol{x}_{k+i+1|k}, \tag{8.3d}$$

$$i = 0, \dots, N-1 \tag{8.3e}$$

where $\boldsymbol{Q} \in \mathbb{R}^{n_y \times n_y}$ is a positive semi-definite state weighting matrix, $\boldsymbol{R} \in \mathbb{R}^{n_r \times n_r}$ is a positive definite invertible control weighting matrix, N is the consider horizon, $\boldsymbol{y}_{k+i|k}$ is the prediction of plant output $\boldsymbol{y}$ based on measurements available at time k, $\bar{\boldsymbol{r}}_k$ is the reference signal for the controlled system at time k and $\boldsymbol{r}_{k+i|k}$ is the input signal for the PI pre-compensated system described by (8.2). Initial minimisation problem (8.3) can be cast in a parametric formulation

$$\min_{\mathbf{z}} \quad \frac{1}{2}\boldsymbol{z}^T\boldsymbol{H}\boldsymbol{z} + \boldsymbol{\rho}_{\boldsymbol{k}}^T\boldsymbol{F}^T\boldsymbol{z} \tag{8.4}$$

with $\boldsymbol{\rho}_{\boldsymbol{k}} \in \mathbb{P}$ the vector of parameters of dimension n_ρ, $\mathbb{P} \subset \mathbb{R}^{n_\rho}$ a bounded set of interest, $\boldsymbol{z} \in \mathbb{R}^{n_z}$ the vector of optimisation variables, $\boldsymbol{H} \in \mathbb{R}^{n_z \times n_z}$ a symmetric and positive definite matrix, $\boldsymbol{F} \in \mathbb{R}^{n_z \times n_\rho}$. The vector of parameters considered in the control of the closed-loop system is

$$\boldsymbol{\rho}_{\boldsymbol{k}} = \begin{bmatrix} \boldsymbol{r}(k-1) & \boldsymbol{x}(k) & \bar{\boldsymbol{r}}(k) \end{bmatrix}.^T \tag{8.5}$$

The explicit solution $\boldsymbol{z}^*$ of the problem (8.5) is analytic and equal to

$$\boldsymbol{z}^* = \boldsymbol{H}^{-1}\boldsymbol{F}\boldsymbol{\rho}_{\boldsymbol{k}}. \tag{8.6}$$

In (8.5) $\boldsymbol{x}(k)$ is the full system state at time k, but in the real plant it is not fully measurable and it is iteratively estimated by a Kalman filter (KF) [87], replacing the true state vector $\boldsymbol{x}(k)$ with its estimate $\hat{\boldsymbol{x}}_{k|k}$ both in the minimisation problem (8.3) and in the control law. Note that $\boldsymbol{H}$ and $\boldsymbol{F}$ matrices are constant and computed offline from $\boldsymbol{A}$, $\boldsymbol{B}$, $\boldsymbol{Q}$ and $\boldsymbol{R}$, and the controller matrices (8.5) are stored and the control law (8.6) computed iteratively avoids to recalculate the solution of (8.4). Considering the state estimation computational effort c_K as in [88], the complexity c of the LQG control law (8.4) can be explicitly computed as

$$c = (2n_p - 1)n_u + c_K. \tag{8.7}$$

The proposed control scheme is presented in Fig. 8.3.

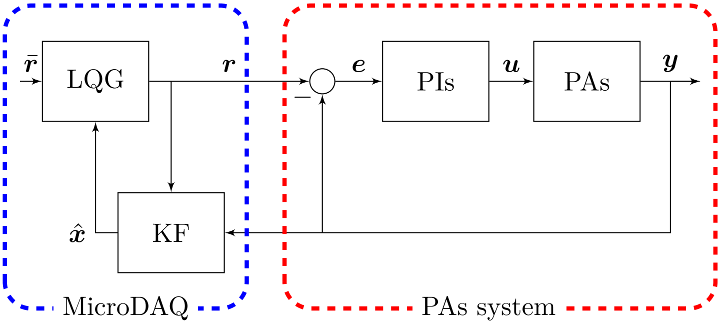
$\bar{\boldsymbol{r}}$
LQG
$\boldsymbol{r}$
$-$
$\boldsymbol{e}$
PIs
$\boldsymbol{u}$
PAs
$\boldsymbol{y}$
$\hat{\boldsymbol{x}}$
KF
MicroDAQ
PAs system

Figure 8.3.: LQG+PI control scheme of the pre-compensated PAs system.

Chapter 9.

Setup and Results

9.1. Experimental setup

Figure 9.1 shows the instrumentation used in the experimental setup. Tests have been performed by the MicroDAQ® E2000 acquisition system by Microdaq. The MicroDAQ provides a Texas Instruments© C6000 DSP core, an ARM9 core and a set of I/O analog ports featured by a maximum sampling frequency of 600 ksps and a resolution of 16 bit. The PA system is composed of a Piezostage (PI P-611.3®) with movement range of 100 [μm] × 100 [μm] × 100 [μm] and 1 [nm] of resolution. The driver moves a Strain Gauge Sensor (SGS) characterised by a resolution on 0.2 [nm]. The MicroDAQ® module is connected to a control amplifier (PI E-505 Amplifier Module®) allowing to generate an adequate control voltage for the PA system amplifying MicroDAQ output control signal from [-1 to 10] [V]to the piezostage input signals range of [-10 to 100] [V]. The amplifier provides an internal set of analog Proportional-Integral (PI) controllers representing the low-level controllers of the PA system.

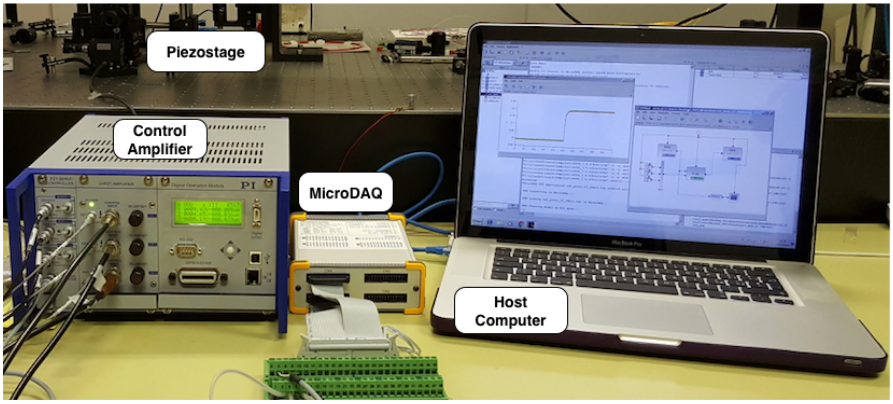

Figure 9.1.: Experimental setup.

9.2. Results

A set of simulation and experimental tests have been considered for the proposed control law. Simulations are realised in the Scilab© simulation environment in order to verify the effectiveness of the controller on the identified model. Test scenario consists into move simultaneously the system by step reference signals of amplitude 0.2 [μm]. The control performances are compared with respect to the results obtained by the provided analog PI controllers. The LQG controller design parameters are reported in Tab. 9.1. The parameters considered in the control performance comparison are: rise time τ_r, settling time τ_s and the Integral Square Error (ISE). Figs. 9.2 and 9.3 present simulation results comparison. In particular, Fig. 9.2 considers simulated controlled output behaviour, showing the slower PI control results with respect to LQG+PI performances. Simulation results are also summarised in Tab. 9.2 showing the considered control performances indices. The LQG policy improves control results, and the faster response is related to a reduced error for each controlled axis, with an average rise time and settling improvement of 60% and 75%, respectively and an average ISE decrease of 60%. In Fig. 9.3 simulated control efforts are presented. Due to the prediction, LQG reference signals present an aggressive behaviour to reduce the rise time and also to limit the output signals overshoot. Experimental results on the real PAs system confirm the performance of simulated controllers. Table 9.3 reports data of experimental step input tests. The LQG+PI controller allows to reduce the rise time of the 25% with respect to PI elapsed time. Also the settling time is improved by the LQG+PI with respect to the PI, reducing the elapsed time of the 29%. The average error computed by the ISE during the transient shows an average reduction of the 40%. Fig. 9.4 presents the controlled real plant outputs comparison. Such as in the simulation tests, the LQG+PI controlled output is driven faster to the reference value with respect to the PIs' signal, avoiding overshoots and oscillations. In Fig. 9.5 the control efforts are reported where the LQG+PI controller presents an initial aggressive behaviour as in the simulated test results.

Table 9.1.: Controller specifications for simulation and experimental tests.

LQG Parameters	**Symbol**	**Value**
Horizon	N	50
Measured variables weights	$\boldsymbol{Q}$	$\boldsymbol{I}(3)$
Manipulated variables rate weights	$\boldsymbol{R}$	$0.95\boldsymbol{I}(3)$
Sample time	T_s	50 μs

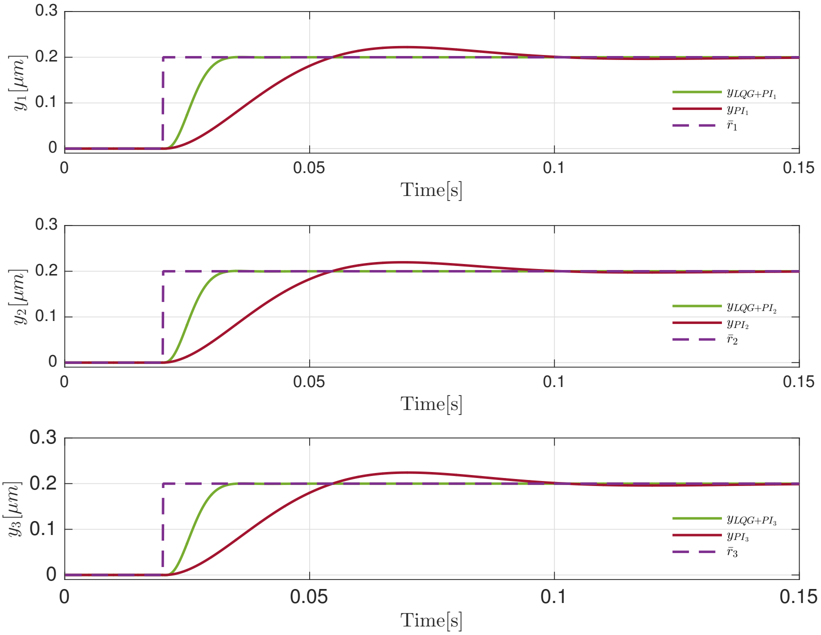

Figure 9.2.: Simulation comparison between PI and LQG+PI outputs.

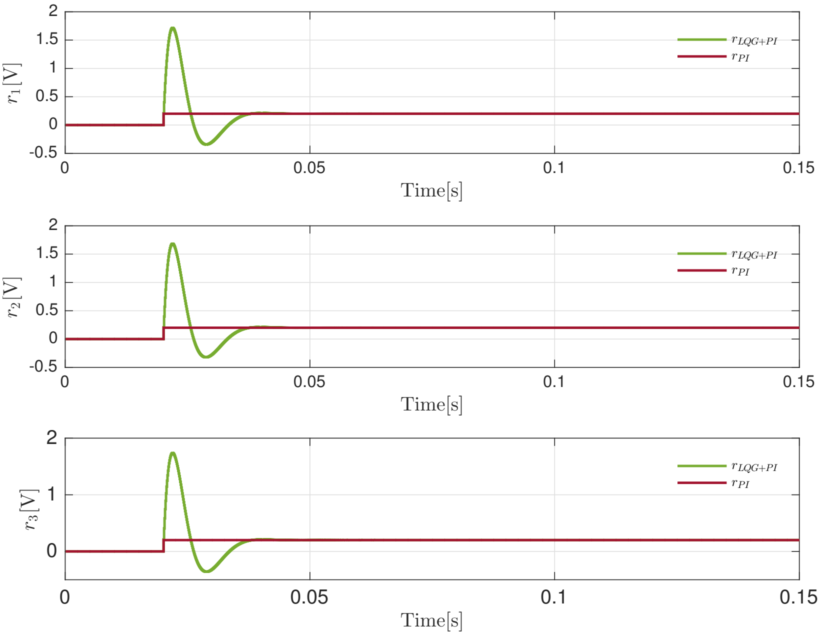

Figure 9.3.: Simulation comparison between PI and LQG+PI control efforts.

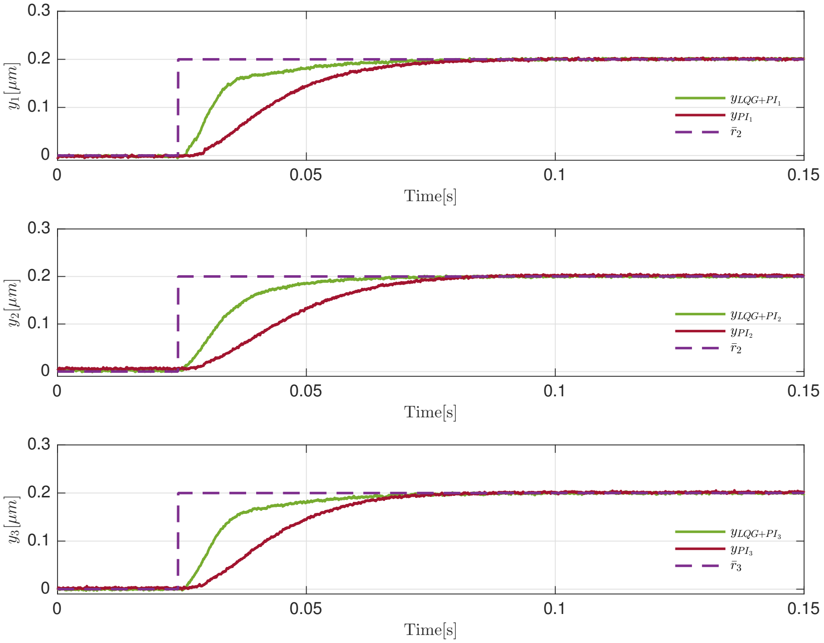

Figure 9.4.: Experimental comparison between PI and LQG+PI outputs.

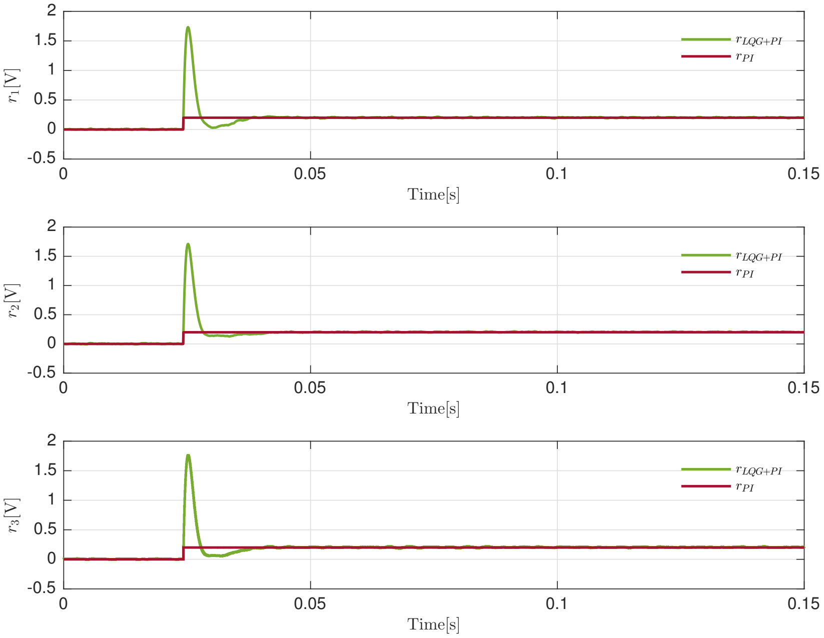

Figure 9.5.: Experimental comparison between PI and LQG+PI control efforts.

Table 9.2.: Simulation results: comparison of PI and LQG+PI under step variations.

		PI	LQG+PI
X axis	$\tau_r[ms]$	0.04	**0.02**
	$\tau_s[ms]$	0.1	**0.025**
	ISE	0.0018	**0.00053**
Y axis	$\tau_r[ms]$	0.04	**0.02**
	$\tau_s[ms]$	0.1	**0.025**
	ISE	0.0017	**0.00050**
Z axis	$\tau_r[ms]$	0.04	**0.02**
	$\tau_s[ms]$	0.1	**0.025**
	ISE	0.0019	**0.00054**

Table 9.3.: Experimental results: comparison of PI and LQG+PI under step variation.

		PI	LQG+PI
X axis	$\tau_r[ms]$	0.065	**0.048**
	$\tau_s[ms]$	0.070	**0.050**
	ISE	0.0011	**0.00045**
Y axis	$\tau_r[ms]$	0.065	**0.045**
	$\tau_s[ms]$	0.070	**0.050**
	ISE	0.0012	**0.0005**
Z axis	$\tau_r[ms]$	0.065	**0.045**
	$\tau_s[ms]$	0.070	**0.050**
	ISE	0.0011	**0.00046**

Chapter 10.

Conclusions

The PhD research activity described in the present dissertation has been developed in the triennium 2015-2018, and it has been sponsored by the Department of Information Engineering of the University “Politecnica Delle Marche” (UNIVPM). Embedded strategies aimed at controlling electromechanical processes have been studied, designed and tested on real systems. The model-based paradigm has been exploited, focusing on both black-box and white-box approaches. Two real processes have been taken into account, represented by *permanent magnet synchronous motor* and *a piezoelectric actuator*. The white-box approach has been applied to the first case study whilst the black-box one the second process. For both systems the literature control solutions have been studied and analysed, highlighting the existent challenges; as a consequence, innovative theoretical ideas have been stated and implemented on embedded boards.

For the *permanent magnet synchronous motor*, an innovative control method has been designed. The main feature of the proposed control solution relies on a tailored algorithm aimed at the on-line computation of winding resistance and the initial angular position. Furthermore, rotor angular position estimation is performed through the exploitation of electrical signals and sensorless speed reference tracking is obtained. A sliding mode control law has been designed in order to obtain robustness to bounded parameter variations affecting the electrical and mechanical system. The developed controller has been installed on a Digital Signal Processing (DSP) board for tracking desired speed reference trajectories. Satisfactory results have been obtained, both from a computational effort point of view and from a disturbance rejections one.

For the piezoelectric actuator, a Linear Quadratic Gaussian (LQG) controller has been designed in order to provide position reference trajectories to a PI controller. The PI controller pre-compensates the considered process. The designed non-invasive control algorithm has been installed on the DSP board. By using the proposed solution, an optimised generation of the PI reference trajectories has been obtained, improving rise time, settling time and position control behaviour. At the same time, the computational effort remains within tolerable margins.

The future work of the present research activity will be focused on the extension of the proposed approach for PMSM winding resistance to another important electrical parameter, *i.e.* the inductance. Furthermore, studies about field-weakening strategies could be performed.

Appendix A.

Tips on PMSM Model Parameters

This appendix is for people like me who came across cryptic datasheets. Not in the sense of unconventional units of measurement, because for these problems there are special conversion tables that through coefficients allow passing between S.I. and not S.I. Units [89], but for ambiguity in how they are measured and between which connectors are measured. In detail, I'll focus on back-EMF constant since the winding inductance "L" and its resistance "R" are easy to test.

A.1. The winding inductance "L" and the resistance "R"

It is well known that the stator windings can be classify as: "Δ" and star "Y" connections. The neutral conductor is almost never available even if the star connection is applied. Thus, without loss of generality, whenever we get a brushless motor in our hands, we can always assume that it connected to a star. It follows that, it is sufficient to measure "R" and "L" between two motor terminals and make sure that the third one is floating, and that the obtained values of "R" and "L" have to be divided by 2.

A.2. bEMF constant

Unlike the parameters described above, the back-EMF constant hides many pitfalls as first of all the name since it is not defined uniquely. in this thesis, a Greek letter "ψ" has been used. "ϕ" or "K_e" mostly used although the worst drawback is how this constant is measured. Just think in which types of voltages between two motor connectors can be measured, *i.e.* peak or RMS values between two phases or phase and neutral. And also how much angular speed units exist, *i.e.* RPM, Hz, rad/s. The math model described in Chapter 4 has been defined using the unit $\frac{\mathrm{V}_{pk,l-to-n}}{\frac{\mathrm{rad_e}}{s}}$ while the more popular unit in the datasheets is $V_{pk,l-to-l}/kRPM$. By Tab. A.1, it is possible to jump from any possible units combination to the right unit adopting a simple conversion factor.

Table A.1.: Converter.

From	*peak* or RMS, $l-to-l$	Conversion factor	To
$\frac{\mathrm{V}}{\mathrm{H}z}$	RMS	$\frac{1}{\pi\sqrt{6}}$	$\frac{\mathrm{V}_{pk,l-to-n}}{\frac{\mathrm{rad}}{s}}$
$\frac{\mathrm{V}}{\frac{\mathrm{r}ad_e}{\mathrm{s}}}$		$\sqrt{\frac{2}{3}}$	
$\frac{\mathrm{V}}{\frac{\mathrm{r}ad_m}{\mathrm{s}}}$		$N_p\sqrt{\frac{2}{3}}$	
$\frac{\mathrm{V}}{k\mathrm{RPM}}$		$\frac{\sqrt{6}}{100\pi N_p}$	
$\frac{\mathrm{V}}{\mathrm{H}z}$	$peak$	$\frac{1}{2\pi\sqrt{3}}$	
$\frac{\mathrm{V}}{\frac{\mathrm{r}ad_e}{\mathrm{s}}}$		$\frac{1}{\sqrt{3}}$	
$\frac{\mathrm{V}}{\frac{\mathrm{r}ad_m}{\mathrm{s}}}$		$\frac{1}{N_p\sqrt{3}}$	
$\frac{\mathrm{V}}{k\mathrm{RPM}}$		$\frac{\sqrt{3}}{100\pi N_p}$	

Bibliography

[1] L. Ljung, “Black-box models from input-output measurements,” in *IMTC 2001. Proceedings of the 18th IEEE Instrumentation and Measurement Technology Conference. Rediscovering Measurement in the Age of Informatics (Cat. No.01CH 37188)*, May 2001, vol. 1, pp. 138–146 vol.1.

[2] D. Liang, J. Li, and R. Qu, “Sensorless control of permanent magnet synchronous machine based on second-order sliding-mode observer with online resistance estimation,” *IEEE Transactions on Ind. Appl.*, vol. 53, no. 4, pp. 3672–3682, July 2017.

[3] V. I. Utkin, J. Guldner, and J. Shi, *Sliding Mode Control in Electromechanical Systems*, CRC Press, 2nd, 2009.

[4] M. Imboden, J. Chang, C. Pollock, E. Lowell, M. Akbulut, J. Morrison, T. Stark, T. G. Bifano, and D. J. Bishop, “High-speed control of electromechanical transduction: Advanced drive techniques for optimized step-and-settle response of mems micromirrors,” *IEEE Control Systems Magazine*, vol. 36, no. 5, pp. 48–76, Oct 2016.

[5] Scilab.io, *Use Case*, 2017 (accessed October 17th, 2018), `http://scilab.io/use-cases-menu/`.

[6] Scilab Enterprices, *Scilab/xCos, License description*, 2017 (accessed October 17th, 2018), `https://www.scilab.org/en/scilab/license`.

[7] Ralph Tyrell Rockafellar, *Convex analysis*, Princeton university press, 2015.

[8] Stephen Boyd and Lieven Vandenberghe, *Convex optimization*, Cambridge university press, 2004.

[9] P. Vas, *Sensorless Vector and Direct Torque Control*, Monographs in electrical and electronic engineering. Oxford University Press, 1998.

[10] W. Fulton, *Algebraic curves: an introduction to algebraic geometry*, Advanced book classics. Addison-Wesley Pub. Co., Advanced Book Program, 1989.

[11] R. Ortega, L. Praly, A. Astolfi, J. Lee, and K. Nam, "Estimation of rotor position and speed of permanent magnet synchronous motors with guaranteed stability," *IEEE Trans. Contr. Sys. Technol.*, , no. 3, pp. 601–614, 2011.

[12] P.P. Acarnley and J.F. Watson, "Review of position-sensorless operation of brushless permanent-magnet machines," *IEEE Trans. Ind. Electron.*, vol. 53, no. 2, pp. 352–362, 2006.

[13] D. Paulus, J.-F. Stumper, and R. Kennel, "Sensorless control of synchronous machines based on direct speed and position estimation in polar stator-current coordinates," *IEEE Trans. Power Electron.*, vol. 28, no. 5, pp. 2503–2513, 2013.

[14] F. Poulain, L. Praly, and R. Ortega, "An observer for PMSM with application to sensorless control," in *Proc. IEEE Conference on Decision and Control*, Cancun, Mexico, dec. 9-11 2008.

[15] M.A. Hamida, J. De Leon, A. Glumineau, and R. Boisliveau, "An adaptive interconnected observer for sensorless control of PM synchronous motors with online parameter identification," *IEEE Trans. Ind. Electron.*, vol. 60, no. 2, pp. 739–748, 2013.

[16] M.A. Hamida, J. de Leon, and A. Glumineau, "Experimental sensorless control for ipmsm by using integral backstepping strategy and adaptive high gain observer," *Contr. Eng. Pract.*, vol. 59, pp. 64 – 76, 2017.

[17] G. Foo and M. F. Rahman, "Sensorless sliding-mode mtpa control of an ipm synchronous motor drive using a sliding-mode observer and hf signal injection," *IEEE Trans. on Ind. Electron.*, vol. 57, no. 4, pp. 1270–1278, April 2010.

[18] S. Bolognani, L. Tubiana, and M. Zigliotto, "Extended Kalman filter tuning in sensorless PMSM drives," *IEEE Trans. Ind. Applicat.*, vol. 39, no. 6, pp. 1741–1747, 2003.

[19] Z. Qiao, T. Shi, Y. Wang, Y. Yan, C. Xia, and X. He, "New sliding-mode observer for position sensorless control of permanent magnet synchronous motors," *IEEE Trans. Ind. Electron.*, vol. 60, no. 2, pp. 710–719, 2013.

[20] H. Kim, J. Son, and J. Lee, "A high-speed sliding-mode observer for the sensorless speed control of a PMSM," *IEEE Trans. Ind. Electron.*, vol. 58, no. 9, pp. 4069–4077, 2011.

[21] A. Astolfi, D. Karagiannis, and R. Ortega, *Nonlinear and adaptive control with applications*, Springer Verlag, Berlin, 2007.

[22] D. Karagiannis, M. Sassano, and A. Astolfi, "Dynamic scaling and observer design with application to adaptive control," *Automatica*, vol. 45, pp. 2883–2889, 2009.

[23] R. Ortega, A. Loria, A.P. Nicklasson, and H. Sira-Ramirez, *Passivity based control of Euler-Lagrange Systems*, Springer Verlag, Berlin, 2007.

[24] J. Lee, J. Hong, K. Nam, R. Ortega, L. Praly, and A. Astolfi, "Sensorless control of surface-mount permanent-magnet synchronous motors based on a nonlinear observer," *IEEE Trans. on Power Electron.*, vol. 25, no. 2, pp. 290–297, 2010.

[25] Osama M. Arafa, Ghada A. Abdel Aziz, Mohamed I. Abu El-Sebah, and Ahmed Aly Mansour, "Observer-based sensorless speed control of PMSM: A focus on drive's startup," *Journal of Electrical Systems and Information Technology*, vol. 3, no. 2, pp. 181 – 209, 2016.

[26] C.M. Verrelli, P. Tomei, E. Lorenzani, G. Migliazza, and F. Immovilli, "Nonlinear tracking control for sensorless PMSM with uncertainties," *Control Engineering Practice*, vol. 60, pp. 157 – 170, 2017.

[27] LI Liu and DA Cartes, "Synchronisation based adaptive parameter identification for permanent magnet synchronous motors," *IET Control Theory & Appl.*, vol. 1, no. 4, pp. 1015–1022, 2007.

[28] Samuel J Underwood and Iqbal Husain, "Online parameter estimation and adaptive control of permanent-magnet synchronous machines," *IEEE Trans. on Ind. Electron.*, vol. 57, no. 7, pp. 2435–2443, 2010.

[29] Thierry Boileau, Nicolas Leboeuf, Babak Nahid-Mobarakeh, and Farid Meibody-Tabar, "Online identification of PMSM parameters: Parameter identifiability and estimator comparative study," *IEEE Trans. Ind. Applicat.*, vol. 47, no. 4, pp. 1944–1957, 2011.

[30] Kan Liu, Zi-Qiang Zhu, and David A Stone, "Parameter estimation for condition monitoring of PMSM stator winding and rotor permanent magnets," *IEEE Trans. on Ind. Electron.*, vol. 60, no. 12, pp. 5902–5913, 2013.

[31] Jin-Woo Jung, Viet Quoc Leu, Ton Duc Do, Eun-Kyung Kim, and Han Ho Choi, "Adaptive PID speed control design for permanent magnet synchronous motor drives," *IEEE Trans. Power Electron.*, vol. 30, no. 2, pp. 900–908, 2015.

[32] Alexey A. Bobtsov, Anton A. Pyrkin, Romeo Ortega, Slobodan N. Vukosavic, Aleksandar M. Stankovic, and Elena V. Panteley, "A robust globally convergent position observer for the permanent magnet synchronous motor," *Automatica*, vol. 61, no. Supplement C, pp. 47 – 54, 2015.

[33] Jose Guadalupe Romero, Romeo Ortega, Zhaoqiang Han, Thomas Devos, and FranÃğois Malrait, "An adaptive flux observer for the permanent magnet synchronous motor," *Int. J. of Adapt. Contr. and Signal Proc.*, vol. 30, no. 3, pp. 473–487, 2016.

[34] Alexey Bobtsov, Anton Pyrkin, and Romeo Ortega, "A new approach for estimation of electrical parameters and flux observation of permanent magnet synchronous motors," *Int. J. of Adapt. Contr. and Signal Proc.*, vol. 30, no. 8-10, pp. 1434–1448, 2016.

[35] Babak Nahid-Mobarakeh, Farid Meibody-Tabar, and F-M Sargos, "Mechanical sensorless control of PMSM with online estimation of stator resistance," *IEEE Trans. Ind. Applicat.*, vol. 40, no. 2, pp. 457–471, 2004.

[36] K. Liu, Z. Q. Zhu, and D. A. Stone, "Parameter estimation for condition monitoring of pmsm stator winding and rotor permanent magnets," *IEEE Trans. on Ind. Electron.*, vol. 60, no. 12, pp. 5902–5913, Dec 2013.

[37] K. Liu and Z. Q. Zhu, "Position-offset-based parameter estimation using the adaline nn for condition monitoring of permanent-magnet synchronous machines," *IEEE Trans. Ind. Electron.*, vol. 62, no. 4, pp. 2372–2383, April 2015.

[38] S. Chi, Z. Zhang, and L. Xu, "Sliding-mode sensorless control of direct-drive pm synchronous motors for washing machine applications," *IEEE Trans. Ind. App.*, vol. 45, no. 2, pp. 582–590, March 2009.

[39] Antti Piippo, Marko Hinkkanen, and Jorma Luomi, "Adaptation of motor parameters in sensorless PMSM drives," *IEEE Trans. Ind. Applicat.*, vol. 45, no. 1, pp. 203–212, 2009.

[40] Sakorn Po-Ngam and Somboon Sangwongwanich, "Stability and dynamic performance improvement of adaptive full-order observers for sensorless PMSM drive," *IEEE Trans. Power Electron.*, vol. 27, no. 2, pp. 588–600, 2012.

[41] Maria Letizia Corradini, G Ippoliti, S Longhi, D Marchei, and G Orlando, "A quasi-sliding mode observer-based controller for PMSM drives," *Asian Journal of Control*, vol. 15, no. 2, pp. 380–390, 2013.

[42] Maria Letizia Corradini and Andrea Cristofaro, "A sensorless speed-tracking controller for permanent magnet synchronous motors with uncertain parameters," in *19th IFAC World Congress, IFAC 2014*, august 2014, vol. 19, pp. 7749–7754.

[43] Andrea Cristofaro, "Uncertain parameter estimation for a class of nonlinear systems using a polynomial representation of outputs," *J. of the Franklin Inst.*, vol. 353, no. 17, pp. 4652–4666, 2016.

[44] D.C. Hanselman, *Brushless Permanent Magnet Motor Design*, Magna Physics Publishing, 2006.

[45] R. J. Walker, *Algebraic curves*, Springer-Verlag, Berlin, 1978.

[46] R. Burden and J. Faires, *Numerical Analysis*, Cengage Learning, 2010.

[47] V. Utkin, J. Guldner, and J. Shi, *Sliding mode control in electromechanical systems*, Systems and Control. CRC Press LLC, 1999.

[48] maxonmotor, *maxon EC-max272769, Datasheet*, 2017 (accessed October 17th, 2018), `https://www.maxonmotor.com/maxon/view/product/272769#`.

[49] Mei-Ju Yang, Guo-Ying Gu, and Li-Min Zhu, "High-bandwidth tracking control of piezo-actuated nanopositioning stages using closed-loop input shaper," *Mechatronics*, vol. 24, no. 6, pp. 724–733, 2014.

[50] Yangmin Li and Qingsong Xu, "A totally decoupled piezo-driven xyz flexure parallel micropositioning stage for micro/nanomanipulation," *IEEE Transactions on Automation Science and Engineering*, vol. 8, no. 2, pp. 265–279, 2011.

[51] YK Yong, SO Reza Moheimani, B J_ Kenton, and KK Leang, "Invited review article: High-speed flexure-guided nanopositioning: Mechanical design and control issues," *Review of scientific instruments*, vol. 83, no. 12, pp. 121101, 2012.

[52] Santosh Devasia, Evangelos Eleftheriou, and SO Reza Moheimani, "A survey of control issues in nanopositioning," *IEEE Transactions on Control Systems Technology*, vol. 15, no. 5, pp. 802–823, 2007.

[53] Andi Sudjana Putra, Sunan Huang, Kok Kiong Tan, Sanjib Kumar Panda, and Tong Heng Lee, "Design, modeling, and control of piezoelectric actuators for intracytoplasmic sperm injection," *IEEE Transactions on Control Systems Technology*, vol. 15, no. 5, pp. 879–890, 2007.

[54] Tomas Tuma, Abu Sebastian, John Lygeros, and Angeliki Pantazi, "The four pillars of nanopositioning for scanning probe microscopy: The position sensor, the scanning device, the feedback controller, and the reference trajectory," *IEEE Control Systems*, vol. 33, no. 6, pp. 68–85, 2013.

[55] Yingfeng Shan and Kam K Leang, "Dual-stage repetitive control with prandtl–ishlinskii hysteresis inversion for piezo-based nanopositioning," *Mechatronics*, vol. 22, no. 3, pp. 271–281, 2012.

[56] Andrzej Milecki and Marcin Pelic, "Application of geometry based hysteresis modelling in compensation of hysteresis of piezo bender actuator," *Mechanical Systems and Signal Processing*, vol. 78, pp. 4–17, 2016.

[57] Henry Frank Tiersten, *Linear Piezoelectric Plate Vibrations: Elements of the Linear Theory of Piezoelectricity and the Vibrations Piezoelectric Plates*, Springer, 2013.

[58] Lei Liu, Yanbin Zhao, Liang Tang, Yufei Xu, Yu-guang Bai, and He Liao, "Modeling and identification investigation of multi-field hysteretic dynamics in flexure-guided piezo platform," *Mechanical Systems and Signal Processing*, vol. 50, pp. 594–606, 2015.

[59] Jack W Macki, Paolo Nistri, and Pietro Zecca, "Mathematical models for hysteresis," *SIAM review*, vol. 35, no. 1, pp. 94–123, 1993.

[60] Mohammed Ismail, Fayçal Ikhouane, and José Rodellar, "The hysteresis bouc-wen model, a survey," *Archives of Computational Methods in Engineering*, vol. 16, no. 2, pp. 161–188, 2009.

[61] Mark A Krasnosel'skii and Aleksei V Pokrovskii, *Systems with hysteresis*, Springer Science & Business Media, 2012.

[62] Qingsong Xu and Minping Jia, "Model reference adaptive control with perturbation estimation for a micropositioning system," *IEEE Transactions on control systems technology*, vol. 22, no. 1, pp. 352–359, 2014.

[63] Zhi Li, Xiuyu Zhang, Chun-Yi Su, and Tianyou Chai, "Nonlinear control of systems preceded by preisach hysteresis description: A prescribed adaptive control approach," *IEEE Transactions on Control Systems Technology*, vol. 24, no. 2, pp. 451–460, 2016.

[64] A. D'Amico, G. Ippoliti, and S. Longhi, "A multiple models approach for adaptation and learning in mobile robots control," *Journal of Intelligent and Robotic Systems: Theory and Applications*, vol. 47, no. 1, pp. 3–31, 2006.

[65] Yangmin Li and Qingsong Xu, “Adaptive sliding mode control with perturbation estimation and pid sliding surface for motion tracking of a piezo-driven micromanipulator,” *IEEE Transactions on Control Systems Technology*, vol. 18, no. 4, pp. 798–810, 2010.

[66] Qingsong Xu, “Piezoelectric nanopositioning control using second-order discrete-time terminal sliding-mode strategy,” *IEEE Transactions on Industrial Electronics*, vol. 62, no. 12, pp. 7738–7748, 2015.

[67] Luca Cavanini, Maria Letizia Corradini, Luigino Criante, Andrea Di Donato, Marco Farina, Gianluca Ippoliti, Sara Lo Turco, Giuseppe Orlando, and Carmine Travaglini, “Robust control of piezostage for nanoscale three-dimensional images acquisition,” in *Industrial Electronics Society, IECON 2016-42nd Annual Conference of the IEEE*. IEEE, 2016, pp. 5107–5112.

[68] M.L. Corradini, G. Ippoliti, and G. Orlando, “Fully sensorless robust control of variable-speed wind turbines for efficiency maximization,” *Automatica*, vol. 49, no. 10, pp. 3023–3031, 2013.

[69] Ning Chuang, Ian R Petersen, and Hemanshu R Pota, “Robust h ∞ control in fast atomic force microscopy,” *Asian Journal of Control*, vol. 15, no. 3, pp. 872–887, 2013.

[70] Peng Chao, Chongwei Han, Jianxiao Zou, and Guanghui Zhang, “H ∞ optimal inversion feedforward and robust feedback based 2dof control approach for high speed-precision positioning systems,” *Journal of Control Science and Engineering*, 2016.

[71] Arnfinn Aas Eielsen, Mernout Burger, Jan Tommy Gravdahl, and Kristin Y Pettersen, “Pi 2-controller applied to a piezoelectric nanopositioner using conditional integrators and optimal tuning,” *IFAC Proceedings Volumes*, vol. 44, no. 1, pp. 887–892, 2011.

[72] Physik Instrumente, *PZ184E User Manual*, Physik Instrumente (PI) GmbH & Co. KG, Auf der Römerstr. 76228 Karlsruhe, Germany, 1.0.0 edition, October 2006.

[73] AM Sadri, JR Wright, and RJ Wynne, “Lqg control design for panel flutter suppression using piezoelectric actuators,” *Smart materials and structures*, vol. 11, no. 6, pp. 834, 2002.

[74] CMA Vasques and J Dias Rodrigues, “Active vibration control of smart piezoelectric beams: comparison of classical and optimal feedback control strategies,” *Computers & structures*, vol. 84, no. 22, pp. 1402–1414, 2006.

[75] MA Trindade, A Benjeddou, and R Ohayon, "Piezoelectric active vibration control of damped sandwich beams," *Journal of Sound and Vibration*, vol. 246, no. 4, pp. 653–677, 2001.

[76] Alberto Bemporad, "Reference governor for constrained nonlinear systems," *IEEE Transactions on Automatic Control*, vol. 43, no. 3, pp. 415–419, 1998.

[77] Alberto Bemporad, Alessandro Casavola, and Edoardo Mosca, "Nonlinear control of constrained linear systems via predictive reference management," *IEEE transactions on Automatic Control*, vol. 42, no. 3, pp. 340–349, 1997.

[78] S Oh and Sunil Kumar Agrawal, "A reference governor-based controller for a cable robot under input constraints," *IEEE transactions on control systems technology*, vol. 13, no. 4, pp. 639–645, 2005.

[79] Shyam Jade, Erik Hellström, Jacob Larimore, Anna G Stefanopoulou, and Li Jiang, "Reference governor for load control in a multicylinder recompression hcci engine," *IEEE Transactions on Control Systems Technology*, vol. 22, no. 4, pp. 1408–1421, 2014.

[80] Luca Cavanini, Gionata Cimini, and Gianluca Ippoliti, "Model predictive control for the reference regulation of current mode controlled dc-dc converters," in *Industrial Informatics (INDIN), 2016 IEEE 14th International Conference on*. IEEE, 2016, pp. 74–79.

[81] Guo-Ying Gu, Li-Min Zhu, Chun-Yi Su, Han Ding, and Sergej Fatikow, "Modeling and control of piezo-actuated nanopositioning stages: a survey," *IEEE Transactions on Automation Science and Engineering*, vol. 13, no. 1, pp. 313–332, 2016.

[82] Matthias Imboden, Jackson Chang, Corey Pollock, Evan Lowell, Mehmet Akbulut, Jessica Morrison, Thomas Stark, Thomas G Bifano, and David J Bishop, "High speed control of electro-mechanical transduction advanced drive techniques for optimized step-and-settle response of mems micromirrors," *arXiv preprint arXiv:1512.05297*, 2015.

[83] Dong Zhang, Cheng-Jin Zhang, Qiang Wei, Yan-Bing Tian, Jing-Bo Zhao, and Xian-Ming Li, "Modeling and control of piezo-stage using neural networks," *Guangxue Jingmi Gongcheng(Optics and Precision Engineering)*, vol. 20, no. 3, pp. 587–596, 2012.

[84] Roel JE Merry, Martijn GJM Maassen, Marinus JG van de Molengraft, Nathan van de Wouw, and Maarten Steinbuch, "Modeling and waveform

optimization of a nano-motion piezo stage," *IEEE/ASME Transactions on Mechatronics*, vol. 16, no. 4, pp. 615–626, 2011.

[85] Georg Schitter and Andreas Stemmer, "Identification and open-loop tracking control of a piezoelectric tube scanner for high-speed scanning-probe microscopy," *IEEE Transactions on Control Systems Technology*, vol. 12, no. 3, pp. 449–454, 2004.

[86] Michael Goldfarb and Nikola Celanovic, "Modeling piezoelectric stack actuators for control of micromanipulation," *IEEE Control Systems*, vol. 17, no. 3, pp. 69–79, 1997.

[87] G. Ippoliti, L. Jetto, and S. Longhi, "Localization of mobile robots: Development and comparative evaluation of algorithms based on odometric and inertial sensors," *Journal of Robotic Systems*, vol. 22, no. 12, pp. 725–735, 2005.

[88] Michel Verhaegen and Paul Van Dooren, "Numerical aspects of different kalman filter implementations," *IEEE Transactions on Automatic Control*, vol. 31, no. 10, pp. 907–917, 1986.

[89] maxonmotor, *maxon DC motor and maxon EC motor, General Information*, 2014 (accessed October 17th, 2018), `https://www.maxonmotor.com/medias/sys_master/root/8815460712478/DC-EC-Key-Information-14-EN-42-50.pdf?attachment=true`.